Please cite this article in press as: Lainšček et al., Decoupling reactogenicity from efficacy enables safer mRNA vaccines, AAV gene delivery, and *in vivo* base editing, Molecular Therapy (2026), https://doi.org/10.1016/j.ymthe.2026.09.033

Molecular Therapy
Original Article

Decoupling reactogenicity from efficacy enables safer mRNA vaccines, AAV gene delivery, and *in vivo* base editing

Duško Lainšček,[1,2,3,8] Špela Malenšek,[1,4,8] Vida Forstnerič,[1,2] Anja Golob-Urbanc,[1] Sara Orehek,[1] Jure Bohinc,[1,4] Mateja Manček Keber,[1] Timotej Sotošek,[1,4] Hana Esih,[1] Peter Pečan,[1,4] Jelica Pantović-Žalig,[1,4] Mojca Benčina,[2] Romina Bester,[5,6] Ulrike Protzer,[5,6,7] and Roman Jerala[1,2]

[1]Department of Synthetic Biology and Immunology, National Institute of Chemistry, 1000 Ljubljana, Slovenia; [2]Centre for Technologies of Gene and Cell Therapy, 1000 Ljubljana, Slovenia; [3]Veterinary Faculty, University of Ljubljana, 1000 Ljubljana, Slovenia; [4]Graduate School of Biomedicine, University of Ljubljana, 1000 Ljubljana, Slovenia; [5]Institute of Virology, Technical University of Munich, School of Medicine and Health, 81675 Munich, Germany; [6]Institute of Virology, Helmholtz Munich, 85764 Munich, Germany; [7]German Center for Infection Research (DZIF), Munich Partner Site, 81377 Munich, Germany

Nucleic acid therapeutics, including mRNA vaccines, genome editors, and viral vectors, are constrained by acute innate reactogenicity that limits dosing flexibility, tissue targeting, and safety. Here, we identify a conserved early innate inflammatory program, peaking approximately 6 h after administration, that governs reactogenicity across mRNA-formulated lipid nanoparticles (LNPs), adenoviral vectors, and AAV9. Using pharmacological and biochemical probes, we show that this program is driven predominantly by nucleic acid cargo sensing, rather than lipid components, and is mechanistically separable from antigen expression, adaptive immune priming, and *in vivo* genome-editing efficacy. Selective modulation of this early cytokine burst achieved here using endosomal nucleic acid-sensing suppressors markedly reduces reactogenicity in multiple mouse models while preserving humoral and cellular immunity to mRNA vaccines, maintaining transgene expression, protecting blood-brain barrier integrity during stereotactic AAV9 delivery, and mitigating LNP-associated hepatotoxicity and thrombocytopenia. These findings define a unifying innate-sensing architecture for nucleic acid therapeutics and establish that reactogenicity is not required for effective vaccination or gene delivery, enabling a broadly applicable strategy to widen the safety window of mRNA medicines, viral vectors, and *in vivo* genome editing.

INTRODUCTION

Nucleic acid (NA)-based therapeutics have progressed from early concepts of gene replacement[1] to a clinically validated modality spanning prophylactic vaccines,[2] oncology,[3] and genome editing for rare and common diseases.[4] The widespread deployment of mRNA-lipid nanoparticle (LNP) vaccines during the COVID-19 pandemic[5,6] and renewed advances in viral vectors have accelerated interest in using NA platforms for both acute and chronic indications. Despite these gains, innate immune sensing of exogenous RNA and DNA remains a central barrier to the safety, tolerability, and dosing flexibility of NA medicines.

Therapeutic NAs are recognized as pathogen-associated molecular patterns by pattern-recognition receptors (PRRs) located in endosomes (TLR3/7/8/9)[7–9] and the cytosol (RIG-I, MDA5, cGAS-STING, AIM2, and NLRs).[6,10] These receptors detect RNA and DNA motifs and trigger inflammatory cytokines, chemokines, and type I IFNs, producing a rapid innate response associated with fever, malaise, myalgia, and, in some settings, organ-specific toxicity.[11–14] While a calibrated innate response may aid vaccine adjuvanticity, excessive or poorly timed activation reduces tolerability, restricts repeat dosing, and can directly impede mRNA translation and stability.[15]

Extensive engineering, such as sequence optimization, high-purity manufacturing, modified caps, and nucleoside analogs such as N1-methylpseudouridine (N1-mΨ),[15–17] has reduced but not eliminated NA sensing. Clinically, even chemically modified mRNA/LNPs cause transient systemic inflammation[11,14,18]; unmodified mRNA is substantially more reactogenic; and viral vectors can induce local or systemic inflammation, including blood-brain barrier (BBB) perturbation after intracerebral administration.[19,20] These liabilities are particularly constraining in high-exposure settings, repeat dosing, and vulnerable tissues such as liver and brain.

Endosomal NA-sensing suppressors, including the clinically established 4-aminoquinolines (e.g., hydroxychloroquine [HCQ]), are

Received 6 January 2026; accepted 21 September 2026;
https://doi.org/10.1016/j.ymthe.2026.09.033.

[8]These authors contributed equally

Correspondence: Roman Jerala, Department of Synthetic Biology and Immunology, National Institute of Chemistry, Hajdrihova 19, 1000 Ljubljana, Slovenia.
E-mail: roman.jerala@ki.si

Published by Elsevier Inc. on behalf of The American Society of Gene and Cell Therapy.
This is an open access article under the CC BY-NC-ND license (http://creativecommons.org/licenses/by-nc-nd/4.0/).

Please cite this article in press as: Lainšček et al., Decoupling reactogenicity from efficacy enables safer mRNA vaccines, AAV gene delivery, and *in vivo* base editing, Molecular Therapy (2026), https://doi.org/10.1016/j.ymthe.2026.09.033

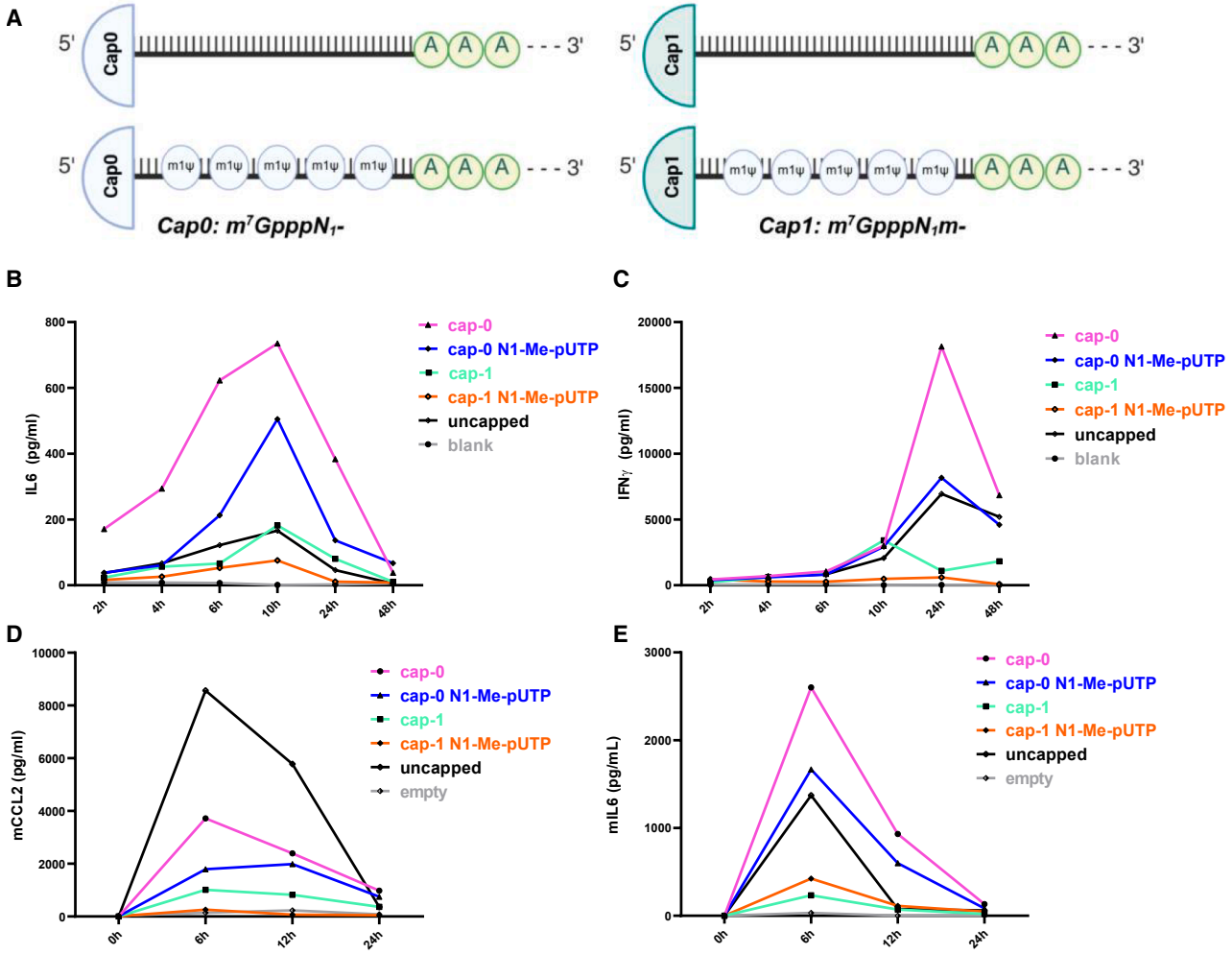


Figure 1. Introduction of mRNA into human cells and mice induces a conserved transient inflammatory spike

(A) PBMC (10^7 cells/mL) electroporation scheme with different mRNA variants (1 μg; firefly luciferase reporter; indicated cap/chemistry). (B and C) Secreted IL-6 (B) and IFNγ (C) at 24 h (n = 3 donors) determined by ELISA. (D and E) Intramuscular LNP-mRNA (5 μg/animal, coding for firefly luciferase) in mice produced a cytokine peak at ~6 h that resolved by 24 h; mouse CCL2 (D) and IL-6 (E) determined in sera by blood draw at depicted time points (n = 3 mice/group). Statistical significance was evaluated by two-way ANOVA with Tukey's comparison test (statistical analysis, see Table S2).

widely used, orally bioavailable agents on the WHO essential medicines list.[21] They reduce NA-PRR engagement through endosomal alkalinization, impaired proteolytic maturation of TLRs, and direct interactions with NAs, thereby limiting receptor accessibility.[22,23] These properties suggest that endosomal NA-sensing suppressors could, in principle, attenuate early reactogenicity across NA delivery platforms without broadly suppressing adaptive immunity.

Here, we test whether selective modulation of early innate NA sensing can enhance the safety of NA therapeutics while preserving efficacy. We evaluate 4-aminoquinolines in the context of mRNA/LNP vaccines, adenoviral vectors, AAV9-mediated CNS gene delivery, and therapeutic mRNA and genome-editing applications. We show that suppressing the early inflammatory spike reduces cytokine surges, rescues LNP-induced hepatotoxicity and thrombocytopenia, and prevents BBB disruption following stereotactic AAV9 (adeno-associated virus 9) delivery. Importantly, antigen expression, neutralizing titers, $CD8^+$ responses, and *in vivo* editing remain intact, demonstrating that reactogenicity is mechanistically separable from efficacy. These findings point to an immediately implementable strategy to broaden the therapeutic window of NA-based medicines.

RESULTS

A conserved, transient inflammatory burst follows NA delivery

We first mapped innate immune responses to mRNA, varying in cap structure and chemical modification. In human peripheral blood mononuclear cells (PBMCs) electroporated with uncapped, cap-0, or cap-1 transcripts ± N1-mΨ (Figure 1A), cap-0 mRNA elicited the highest IL-6 and IFNγ, followed by cap-0 N1-mΨ mRNA and uncapped mRNA. The cap-1 and cap-1 N1-mΨ mRNA produced

Please cite this article in press as: Lainšček et al., Decoupling reactogenicity from efficacy enables safer mRNA vaccines, AAV gene delivery, and *in vivo* base editing, Molecular Therapy (2026), https://doi.org/10.1016/j.ymthe.2026.09.033

substantially lower but still detectable signals (Figures 1B and 1C). Time-course analysis showed cytokines rising by 3 h, peaking at ∼24 h for IFNγ and at 10 h for IL-6 after electroporation, and diminishing by 48 h for IL-6, whereas IFNγ was still measurable after 48 h for most mRNA variants. To capture physiological NA delivery, we formulated the same transcripts in LNPs and injected mice with LNPs intramuscularly. Serum IL-6 and CCL2 surged at ∼6 h and returned to baseline by 24 h (Figures 1D and 1E). Similar to PBMCs, cap-0 mRNAs were highly reactogenic, whereas uncapped mRNAs gave the highest CCL2 response in animals, yet the highest IL-6 cytokine peak was observed for the LNPs delivering cap-0 mRNA. N1-mΨ-modified and cap-1 mRNAs produced a smaller yet still substantial spike. The conserved ∼6 h peak suggested a shared early innate program triggered across modalities and delivery routes. Vehicle and empty LNPs produced negligible cytokine changes at matched volumes.

Endosomal NA-sensing suppressors blunt inflammation and preserve adaptive immunity to mRNA vaccines

We next assessed whether 4-aminoquinoline-based endosomal NA-sensing suppressors directly interact with NAs and LNP vaccine particles. We showed previously that chloroquine (CQ) and other imidazoquinolines inhibit activation of endosomal TLRs through interaction with NAs.[23] HCQ binds to the minor groove of DNA or by intercalation, depending on concentration.[24] Binding of HCQ to different types of RNAs, DNAs, and NA delivery particles (LNP mRNA-based vaccine and adenovirus DNA-based vaccine) was tested by intrinsic fluorescence and competition with propidium iodide (PI) (Figure S1). As LNPs emerged as efficient delivery vehicles for NAs,[25] the effect of HCQ was studied also on mRNA, encapsulated into LNPs, to assess its interaction with the formulation and its effect on LNP integrity. Titration revealed a concentration-dependent decrease of HCQ fluorescence intensity upon the addition of double-stranded DNA (dsDNA) (Figure S1C). Competition with PI demonstrated that HCQ competes for binding to dsDNA (Figure S1D). Interaction of HCQ was observed with both dsRNA and single-stranded RNA (ssRNA) (Figures S1E and S1F). In contrast, addition of both empty and mRNA-containing LNPs resulted in increased HCQ fluorescence (Figures S1G and S1H), indicating that HCQ also associates with the LNP carrier and that this interaction cannot be attributed specifically to the encapsulated mRNA. We additionally observed an increase in fluorescent intensity of HCQ (1 mM) after the gradual addition of AZD1222, a DNA-based adenoviral vaccine, or LNP-mRNA-based BNT162b2, a COVID vaccine[5] (Figures S1I and S1J). Dynamic light scattering confirmed that adding these agents to LNP formulations preserved particle size and polydispersity, indicating no disruption of the delivery vehicles (Figures S1K–S1O). Together, these results demonstrate direct interaction of HCQ with NAs and an association with the LNP carrier.

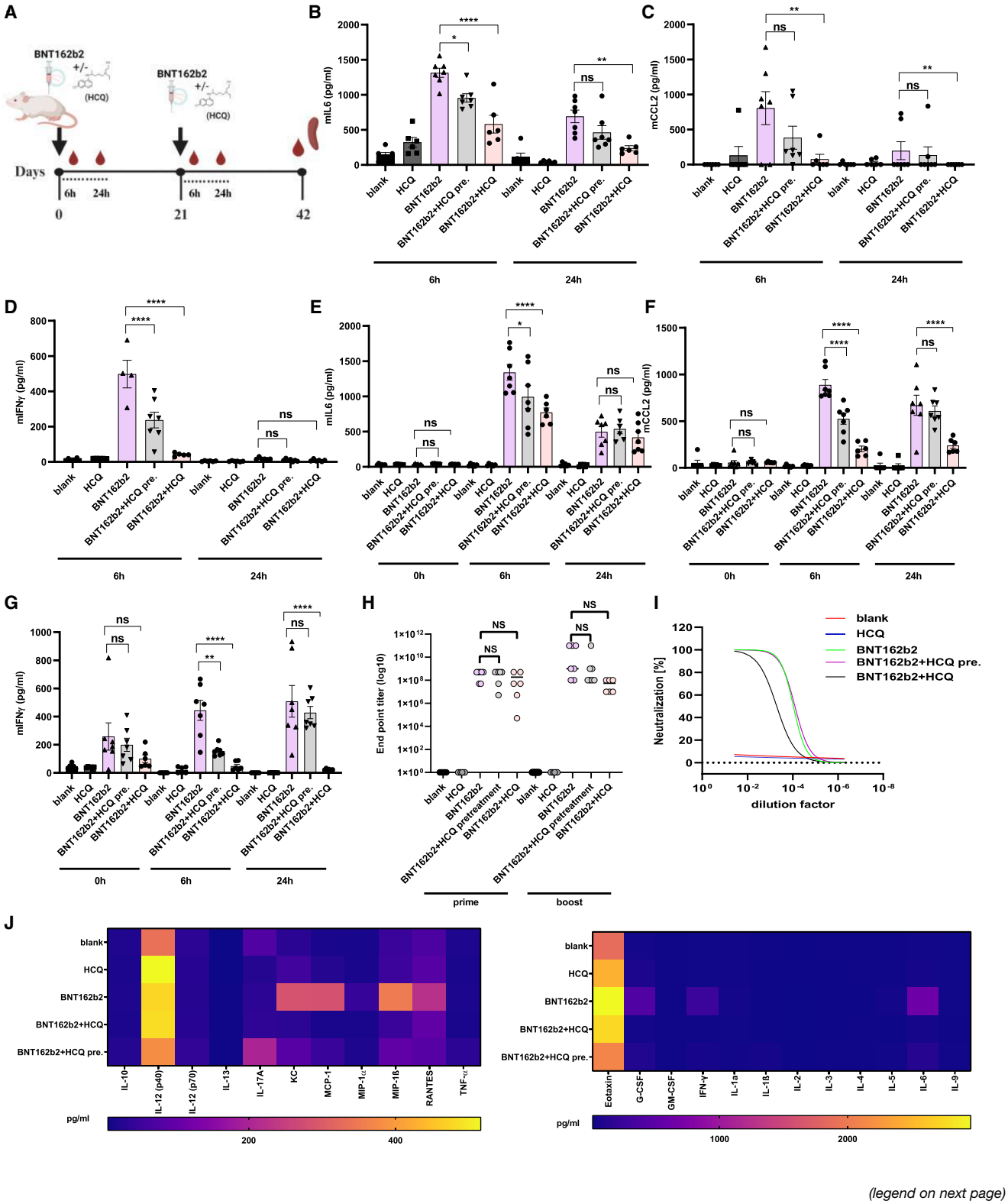
In PBMCs, endosomal NA-sensing suppressors markedly reduced IFNγ after electroporation of diverse mRNAs. Under the same conditions, bafilomycin A1 (BafA1), an endosomal acidification inhibitor,[26] mostly did not suppress cytokine production, consistent with cytosolic entry bypassing endosomes. Importantly, the effect of HCQ was retained when mRNA was delivered directly into the cytosol in the absence of LNPs, demonstrating that its anti-inflammatory activity is not dependent on interaction with the lipid carrier and, together with the direct NA-binding experiments, is consistent with a contribution of direct NA interaction to the observed effect (Figures S2A–S2E). In mice, co-formulating these suppressors with LNP/mRNA strongly reduced the 6 h cytokine burst (Figures S2F–S2O). Additionally, pharmacological congeners (CQ and quinacrine [Q]) produced similar cytokine reductions (IL-6) in PBMCs, electroporated with different fLUC (firefly luciferase) mRNAs (Figure S2P), suggesting a class effect among 4-aminoquinolines.

We next inquired if the addition of 4-aminoquinolines could negatively influence the translation of the protein of interest. By measuring the bioluminescence signal in electroporated PBMCs, we found that HCQ treatment did not negatively affect protein synthesis under the tested conditions (Figure S3A; Table S2). Although CQ and Q reduced protein expression under specific conditions, these compounds were not used in subsequent experiments, which focused specifically on HCQ (Figure S3A; Table S2). An LDH (lactate dehydrogenase) assay confirmed the lack of influence of pharmacological congeners on cell viability (Figure S3B). The same approach for determining targeted protein translation by measuring bioluminescence was applied *in vivo*. In all animals, we determined that the addition of HCQ does not impair fLUC protein translation of different variants of mRNA delivered via LNPs (Figure S3C). Finally, we performed an *in vitro* translation assay and yet again confirmed the lack of influence of HCQ on protein translation (Figure S3D).

We next evaluated clinically relevant mRNA vaccines. BNT162b2 induced the characteristic ∼6 h cytokine peak in PBMCs that was also observed after 24 h (Figure S4A). The same IL-6 and CCL2 ∼6 h burst was also observed in mice, which were given the COVID-19 vaccine intramuscularly (Figures S4B and S4C). Endosomal NA-sensing suppression substantially reduced IL-6 and CCL2 in mice (Figures S4B and S4C), as also shown for human cells. In PBMCs exposed to BNT162b2, the addition of BafA1 also lowered cytokines, consistent with the endocytic uptake route (Figure S4A). Similar to HCQ, CQ and Q significantly reduced IL-6 cytokine in PBMCs upon BNT162b2 treatment, suggesting a potent role of 4-aminoquinolines in NA-induced inflammation (Figure S4D).

To test a more stringent condition, we immunized mice with unmodified cap-0 spike mRNA/LNP, which is more reactogenic than N1-mΨ mRNA. Suppression of the cytokine peak was potent at both prime and boost (Figures S4E–S4J) in animals that received a co-formulation of spike mRNA/LNPs and HCQ, and the titers of spike-specific IgG were unchanged, whereas we observed a slight reduction in $CD8^+$ cytotoxicity against spike-pseudovirus-infected targets (Figures S4K–S4M). Spectral flow cytometry of spleen cells, isolated from the spleen of immunized animals on day 42, confirmed similar frequencies of activated $CD44^+$, $CD8^+$,

Please cite this article in press as: Lainšček et al., Decoupling reactogenicity from efficacy enables safer mRNA vaccines, AAV gene delivery, and *in vivo* base editing, Molecular Therapy (2026), https://doi.org/10.1016/j.ymthe.2026.09.033



(legend on next page)

and B cell subsets ($CD86^{high}MHCII^{high}$ and $CD62L^{high}MHCII^{high}$) (Figures S4N and S4O).

For BNT162b2, we compared LNP/mRNA co-formulation with administration 24 h before vaccination (prophylaxis) *in vivo*; therefore, mice were injected with HCQ 24 h prior to the BNT162b2 immunization (HCQ-pre), whereas another group of animals received a co-formulation of HCQ and BNT162b2, meaning that vaccine and suppressor were mixed into a single injection, given intramuscularly (BNT162b2+HCQ). This was done on day 0 (prime dose), which was repeated with a boost dose (21 days after the first dose). Blood was taken 6 and 24 h post-immunization. On day 42, the animals were sacrificed, and samples were subjected to further analysis (Figure 2A). Both regimens reduced IL-6, CCL2, and IFNγ at prime and boost (Figures 2B–2G), with co-formulation providing the most pronounced suppression. Endpoint spike-binding titers remained unchanged (Figure 2H). Neutralization IC_{50} values of live SARS-CoV-2 virus by immunized mice, which received a single co-formulation, were lower compared to vaccine-injected mice only when the HCQ was given as prophylaxis (Figures 2I and S5). Multiplex analysis confirmed broad reductions in eotaxin, G-CSF, IFNγ, IL-5, IL-6, IL-12p40, KC, MCP-1, MIP-1α/β, and RANTES at 6 h (Figures 2J, S6A, and S6B).

Performing a co-culture assay of SARS-CoV-2 pseudovirus-infected NIH 3T3 cells with spleen $CD8a^+$ isolated T cells from fully immunized animals, the cytotoxicity was tested, which was also higher for animals that received HCQ (Figures 3A–3D). Cytometry analysis of bulk spleen cell suspension revealed an increase of $CD4^+$ T cells in all immunized animals. The $CD8^+$ population was also increased in HCQ-pre groups, whereas we observed a lower number of cytotoxic T cells in animals that received a co-formulation of vaccine and HCQ. Flow cytometric analysis demonstrated that the overall frequency of B cells remained comparable across all experimental groups. Likewise, the proportion of $MHCII^{high}$ B cells, representing B cells with a prominent antigen-presenting phenotype, was not significantly altered following BNT162b2 immunization, either alone or in combination with HCQ. The frequency of $MHCII^{high}CD38^{high}$ B cells, corresponding to mature antigen-presenting B cells, was maintained across all immunized groups and showed a modest increase in animals receiving BNT162b2 together with HCQ. In contrast, the frequency of $CD38^{high}$ B cells, representing mature non-germinal-center B cells, displayed greater inter-animal variability without consistent differences between treatment groups. Similarly, the $CD24^{med}MHCII_{high}CD38^{high}$ B cell population, consistent with mature antigen-presenting B cells, remained abundant and comparable across all experimental groups (Figures 3E–3G and S6C).

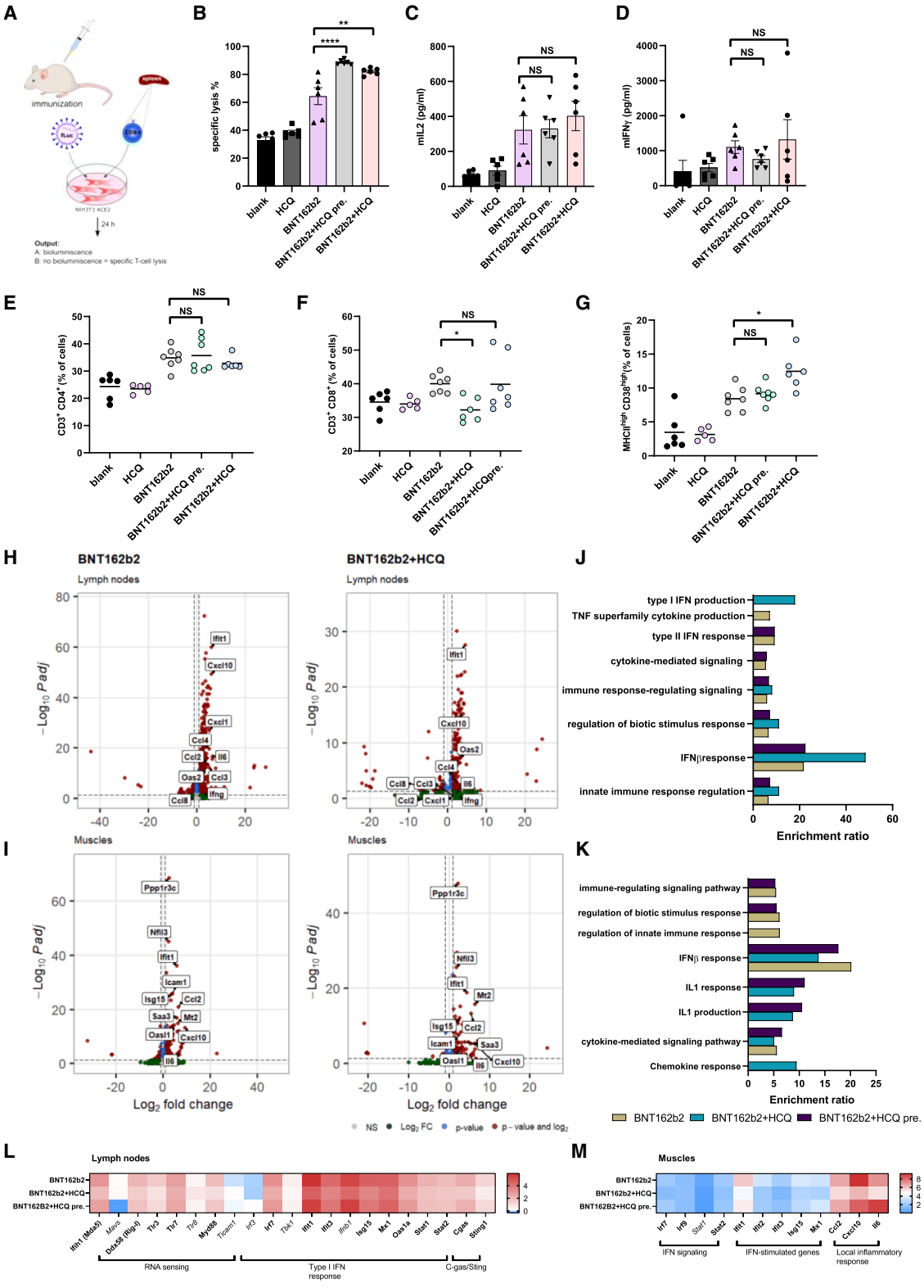
Bulk RNA sequencing (RNA-seq) of draining lymph nodes (Figure 3H) and peri-injection muscle (Figure 3J) at 3 h post-injection to determine the early transcriptomic changes[27] (Figure S6D) revealed distinct innate activation signatures in vaccine-only animals, which were selectively dampened by NA-sensing suppression, seen in lymph nodes (Figures 3H–3J, 3L, and S6E) and in muscles (Figures 3I–3K and 3M). BNT162b2 vaccination induced distinct innate immune activation in both tissues, with a prominent RNA-sensing and IFN-responsive signature in lymph nodes (Figure 3L) and a strong IFN-stimulated and local inflammatory response at the infection site (Figure 3M). In the lymph nodes, RNA-sensing genes included upregulation of *Tlr3*, *Tlr7*, *Ddx58* (*Rig*-I), *Ifih1* (*Mda5*), and *Myd88* with robust changes in IFN response, including *Irf7*, *Ifit1*, *Ifit3*, *Isg15*, and *Mx1*. The response was attenuated by HCQ treatment, although substation induction persisted following HCQ pretreatment. *cGas* and *Sting1* were also induced; however, these changes are interpreted as cGAS-STING transcriptional response rather than evidence of primary pathway activation. In peri-injection muscle, BNT162b2 elicited a pronounced local inflammatory response, also driven by IFN-stimulated genes, including *Ifit1*, *Ifit2*, *Ifit3*, *Isg15*, *Mx1*, *Cxcl10*, *Ccl2*, and *Il6* (Figure 3M). Addition of HCQ blunted the magnitude of several of these responses, with prophylaxis showing intermediate effects (Figures 3L and 3M). Clinical blood markers of immunized animals remained unchanged (Figure S6F).

As the adaptive immune response matures over time, we next investigated whether HCQ co-administration could adversely affect the long-term development of vaccine-induced immunity. To address this, mice were immunized using the same prime-boost regimen with a co-formulation of BNT162b2 and HCQ, and the study was extended to 84 days following the primary immunization to enable long-term assessment of adaptive immune responses. In addition, a separate cohort of mice was euthanized on day 42, corresponding to the original study endpoint, to allow direct comparison between the short- and long-term immune responses. Finally, an additional group of animals was included in which BNT162b2 and HCQ were administered into contralateral hindlimbs to determine whether spatial separation of the two components preserves the anti-inflammatory effect of HCQ while minimizing potential effects on vaccine immunogenicity (Figure S7A). Again, reduced cytokine levels were observed in animals receiving the co-formulation of the vaccine and HCQ. Importantly, contralateral administration of HCQ likewise significantly decreased mIL-6 and mIFNγ levels after both the prime and booster immunizations (Figures S7B–S7G), demonstrating that the anti-inflammatory effect of HCQ is maintained even when administered separately from the vaccine and therefore does not require physical co-formulation

Figure 2. Endosomal nucleic acid-sensing suppression attenuates BNT162b2 reactogenicity without compromising humoral immunity

(A) Immunization scheme for BNT162b2 intramuscular immunization (4 μg) at days 0 (prime dose) and 21 (booster dose); suppressor (HCQ; 60 mg/kg body weight) co-formulated with BNT162b2 or given 24 h prior (as a prophylaxis). (B–G) Mouse serum IL-6, CCL2, and IFNγ, determined by ELISA at 6/24 h after prime (B–D) and boost (E–G) dose. (H) Endpoint anti-Spike IgG titers (prime and boost). (I) Live SARS-CoV-2 neutralization (IC_{50}) by mouse sera obtained from immunized animals. (J) Multiplex chemokine/cytokine panel at 6 h post-immunization ($n = 6$). Graphs present mean values ± SEM. Each dot represents a value obtained from an individual animal ($n = 6$). $^*p < 0.05$, $^{**}p < 0.01$, $^{***}p < 0.001$, and $^{****}p < 0.0001$. All p values are from ordinary one-way ANOVA followed by Tukey's multiple comparisons test.

Please cite this article in press as: Lainšček et al., Decoupling reactogenicity from efficacy enables safer mRNA vaccines, AAV gene delivery, and *in vivo* base editing, Molecular Therapy (2026), https://doi.org/10.1016/j.ymthe.2026.09.033



(legend on next page)

or spatial co-localization of the two components. This is consistent with the extensive systemic tissue distribution and lysosomal accumulation of HCQ[28,29] and with the drainage of mRNA-LNP vaccines to draining lymph nodes and secondary lymphoid organs beyond the injection site,[30,31] where both components can converge within the endosomal compartments of antigen-presenting cells. Anti-spike IgG endpoint titers (EPTs) were comparable across all groups receiving HCQ. Although a modest reduction in antibody titers was observed in the group receiving HCQ via contralateral hindlimb administration, this difference did not reach statistical significance compared to the vaccine-only group (Figure S7H). Endpoint analysis of splenocytes collected on day 42 revealed comparable frequencies of activated $CD44^+$ $CD4^+$ and $CD8^+$ T cells across all groups, indicating similar generation of antigen-experienced T cell populations following immunization (Figures S7I and S7J). Likewise, the frequencies of $CD19^+CD86^+$ B cells were comparable between groups, demonstrating that HCQ did not impair B cell activation induced by vaccination (Figure S7K). To determine whether HCQ affects the long-term development of adaptive immunity, a second cohort of animals was analyzed 84 days after primary immunization while following the same prime-boost vaccination regimen as the short-term cohort. As expected, circulating cytokine levels returned to baseline by the study endpoint (Figures S7L–S7N). Importantly, anti-spike IgG EPTs remained robust and comparable across all experimental groups (Figure S7O). Likewise, the frequencies of activated $CD44^+$ $CD4^+$ and $CD8^+$T cells, as well as $CD19^+CD86^+$ B cells, were similar between groups (Figures S7P–S7S), demonstrating that HCQ co-administration does not compromise the long-term development of either cellular or humoral immunity. Together, these results indicate that the pronounced early inflammatory spike is not required for effective priming and that selective suppression of early sensing preserves antigen expression and adaptive immunity.

Mechanistic characterization of HCQ-mediated selective suppression of NA sensing

To define the potential mechanism underlying HCQ-mediated suppression of NA-induced inflammation, we investigated whether HCQ acts by directly inhibiting innate immune signaling pathways or by preventing immunostimulatory NAs from engaging their cognate PRRs. Human PBMCs were therefore stimulated with BNT162b2 vaccine or various agonists, selectively activating distinct innate immune pathways. Consistent with our previous observations, not only did BNT162b2 induce robust secretion of IL-6, CCL2, and IFNγ, but we also observed an induction of IL-8, TNFα, and IFNβ, all of which were significantly attenuated by HCQ treatment (Figures S8A–S8E). Importantly, HCQ failed to suppress cytokine production induced by the non-NA TLR7/8 agonist R848 or the direct STING agonist cGAMP, indicating that its anti-inflammatory activity is not mediated by broad inhibition of innate immune signaling but rather by selective interference with NA sensing. In contrast, HCQ efficiently reduced cytokine responses elicited by polyI:C, a synthetic dsRNA analog that requires NA recognition for immune activation, further supporting the mechanism based on shielding of immunostimulatory NAs (Figures S8A–S8E). To further investigate whether early inflammatory cytokines actively contribute to the downstream reactogenic cytokine network, IL-6 and IFNγ were individually neutralized during BNT162b2 stimulation of human PBMCs. As expected, anti-IL-6 and anti-IFNγ antibodies efficiently depleted detectable IL-6 and IFNγ from culture supernatants (Figures S8F and S8G). Importantly, neutralization of either IL-6 or IFNγ significantly reduced CCL2 secretion (Figure S8H), consistent with previous reports describing interactions between IL-6, IFNγ, and CCL2 signaling pathways.[32,33] These findings provide functional evidence that both cytokines contribute to the amplification of the early inflammatory response induced by mRNA/LNPs rather than merely serving as correlative biomarkers of innate immune activation. In order to determine whether HCQ modulates early innate immune signaling, we employed a dual-reporter A549 cell line expressing secreted embryonic alkaline phosphatase (SEAP) under the control of NF-κB-responsive elements and Renilla luciferase (rLUC) under the control of an IRF3-responsive promoter, two principal signaling pathways downstream of innate NA sensing. While HCQ did not significantly reduce NF-κB- or IRF3-dependent reporter activity, a consistent reduction in both SEAP and rLUC signals was observed following co-treatment with BNT162b2 or the NA agonist polyI:C. In contrast, HCQ had no detectable effect on reporter activation induced by the direct STING agonist cGAMP (Figures S8I and S8J).

Prompted by the observed trend toward reduced SEAP and rLUC reporter activity, we next investigated activation of the NF-κB and IRF3 signaling pathways in human PBMCs stimulated with BNT162b2. Immunoblot analysis demonstrated rapid activation

Figure 3. Adaptive T cell responses remain intact, while early innate signaling programs are selectively dampened

(A) Cytotoxic T cell killing, isolated from prime- and boost-immunized mice (depicted in Figure 2A at day 42) spleens, against cells expressing viral S protein. The cytotoxic effect of isolated vaccinated mouse spleen $CD8a^+$ T cells was determined on pseudovirus-infected hACE2 and TMPRSS2-transfected NIH 3T3 cells. Bioluminescence was determined 24 h post-co-culture of murine spleen cells with NIH 3T3 cells. Based on radiance values obtained from pseudovirus infection, specific lysis of NIH 3T3 cells was calculated. (B–D) $CD8^+$-specific cytolysis (B) and mouse IL-2 (C) and IFNγ (D) production from co-cultures of immunized mouse splenocytes with spike-pseudovirus-infected targets. (E–G) Spectral flow cytometry of splenocytes ($CD4^+$, $CD8^+$, $MHCII^{high}CD38_{high}$) on day 42, isolated from the immunized animals. (H and I) Enhanced volcano plots of differentially expressed genes in lymph nodes (H) and muscle (I), where the RNA for bulk RNA-seq was isolated from the tissue, 3 h post-immunization. (J and K) Over-representation analysis of upregulated pathways for lymph nodes (J) and muscles (K). (L and M) Heatmap of pathway genes for lymph nodes (L) and muscle samples (M). Each dot represents a value obtained from an individual animal ($n = 6$). $^*p < 0.05$, $^{**}p < 0.01$, $^{***}p < 0.001$, and $^{****}p < 0.0001$. All p values are from ordinary one-way ANOVA followed by Tukey's multiple comparisons test compared to blank.

Please cite this article in press as: Lainšček et al., Decoupling reactogenicity from efficacy enables safer mRNA vaccines, AAV gene delivery, and *in vivo* base editing, Molecular Therapy (2026), https://doi.org/10.1016/j.ymthe.2026.09.033

of both pathways following vaccine stimulation, as evidenced by increased phosphorylation of NF-κB (pNF-κB) and IRF3 (pIRF3) within 15–30 min after stimulation (Figure S9A). Co-administration of HCQ markedly attenuated phosphorylation of both signaling molecules. Quantification of band intensities confirmed a substantial reduction in the ratios of pNF-κB and pIRF3 relative to total protein at the early time points following stimulation (Figure S9B).

Because endosomal acidification is required for the maturation and activation of endosomal NA-sensing receptors, including TLR3, TLR7, and TLR9, we next investigated whether HCQ alters endosomal pH, as this is also one of the proposed mechanisms of HCQ.[34] HEK293 cells were co-labeled with low-molecular-weight dextran dyes: a pH-sensitive fluorophore, FITC-dextran, whose fluorescence increases with increasing pH, and Alexa Fluor 647 (AF647)-dextran, which serves as a pH-insensitive reference signal. Endosomal pH was therefore quantified using the ratio of both dyes' fluorescence within individual endosomal regions of interest (ROIs) identified by automated image analysis (Figure S10A). HCQ treatment significantly reduced the FITC/AF647 fluorescence ratio compared with untreated cells (Figure S10B), indicating reduced endosomal acidification and a relative increase in endosomal pH. Together, these data support a model in which HCQ elevates endosomal pH, thereby limiting NA sensing and selectively reducing NA-driven inflammatory signaling without broadly suppressing downstream immune pathways.

Mitigation of adenoviral vector reactogenicity with preserved efficacy

Because HCQ binds NAs, we next investigated whether it could similarly mitigate the innate inflammatory response elicited by the chimpanzee adenoviral vector vaccine AZD1222[35] without compromising vaccine-induced immunity. Mice were immunized using a prime-boost regimen with an 8-week interval between doses (Figure S11A). HCQ co-administration significantly reduced circulating IL-6, CCL2, and IFNγ levels following both the prime and booster immunizations. Importantly, both contralateral administration of HCQ and 24-h prophylactic treatment similarly attenuated cytokine induction, further supporting the ability of HCQ to shield NA-induced innate immune activation independently of co-formulation with the vaccine (Figures S11B–S11G). Spike-reactive antibody titers and neutralization remained unchanged (Figures S11H–S11J and S12), and CD8a cytotoxic T cell responses were preserved in all tested animal groups (Figures S11K–S11M). Endpoint flow cytometric analysis of splenocytes collected 16 weeks after primary immunization revealed a modest reduction in the frequency of $CD4^+$ T cells in HCQ-treated animals. In contrast, HCQ administration was associated with a slight increase in the proportion of $CD8^+$ T cells and $CD3^+CD8^+CD62L^+$ cells, suggesting preservation of a less-differentiated $CD8^+$ T cell phenotype without compromising the overall adaptive immune response (Figures S11N–S11P).

Endosomal NA-sensing suppression rescues AAV-induced BBB damage

Direct intracerebral AAV9 delivery, used for multiple neurological indications,[36] can disrupt the BBB and induce neuroinflammation.[37–39] We implemented a prophylactic regimen (daily for 3 days before and 2 days after injection) and stereotactically delivered AAV9-EGFP to the mouse cortex (Figure 4A). IL-6 was reduced on days 1 and 30, at the end of the experiment, compared to AAV9 alone, and EGFP transduction efficiency was preserved (Figures 4B and S13C). Immunohistochemistry on day 30 revealed BBB injury in AAV9-only brains: reduced CD31, diminished AQP4, increased $IBA1^+$ microglia and $GFAP^+$ astrocytes, and lower NeuN (Figures 4C–4E and S13D). Endosomal NA-sensing suppression preserved CD31 and AQP4, reduced microgliosis and astrocytosis, and maintained NeuN abundance (Figures 4E and S13D). Thus, selective early innate modulation safeguards vascular and glial homeostasis during intracerebral AAV9 administration without compromising transduction efficiency.

Amelioration of LNP-mRNA hepatotoxicity and thrombocytopenia and support for base-editor dosing

LNP/mRNA exposure often concentrates in the liver, where dose-dependent hepatotoxicity[40–42] and thrombocytopenia can limit repeated treatment and even result in a clinical trial pause.[43] Using cap-1 N1-mΨ-modified mRNA erythropoietin (EPO) LNPs, we confirmed therapeutic expression, with serum EPO increasing appropriately and unaffected by NA-sensing suppression. A separate cohort of animals receiving fLUC mRNA/LNPs was included as a control group (Figures 5A and S14A). IL-6 and CCL2 levels measured 6 h after administration were markedly reduced in all HCQ-treated groups following both the initial and subsequent administrations of low- (0.2 mg/kg) and high- (1 mg/kg) dose LNPs (Figures 5B, 5C, S14B, and S14C). Animals treated with EPO mRNA/LNPs exhibited significantly elevated hematocrit levels compared with the control group (Figures 5D and S14D). Administration of the low mRNA-LNP dose did not result in significant alterations in liver function parameters (Figure S14E). Dose escalation of EGFP mRNA-LNPs (0.2–1.5 mg/kg) revealed consistent cytokine peaks 6 h after administration (Figure S14H). At doses of 1.0–1.5 mg/kg, significant elevation in serum ALT and AST levels was observed, whereas no such changes occurred following administration of empty LNPs (Figures 5E, 5F, and S14I–S14L), indicating that the observed hepatotoxicity was driven by the NA cargo rather than the LNP formulation itself. Suppression of early innate sensing blunted cytokines and reduced ALT/AST elevations across reporters and EPO (Figures 5E, 5F, and S14I), with histology showing fewer inflammatory foci and reduced hepatocyte injury (Figures 5G and S14L). Complete blood counts showed mitigation of LNP-mRNA-induced thrombocytopenia while preserving EPO-driven erythropoiesis (Figures S15A–S15J).

A prominent application of mRNA therapeutics is *in vivo* genome editing.[44,45] Editing *Pcsk9* provides durable LDL reduction[41] and protects against cardiovascular disease, representing a highly

Please cite this article in press as: Lainšček et al., Decoupling reactogenicity from efficacy enables safer mRNA vaccines, AAV gene delivery, and *in vivo* base editing, Molecular Therapy (2026), https://doi.org/10.1016/j.ymthe.2026.09.033

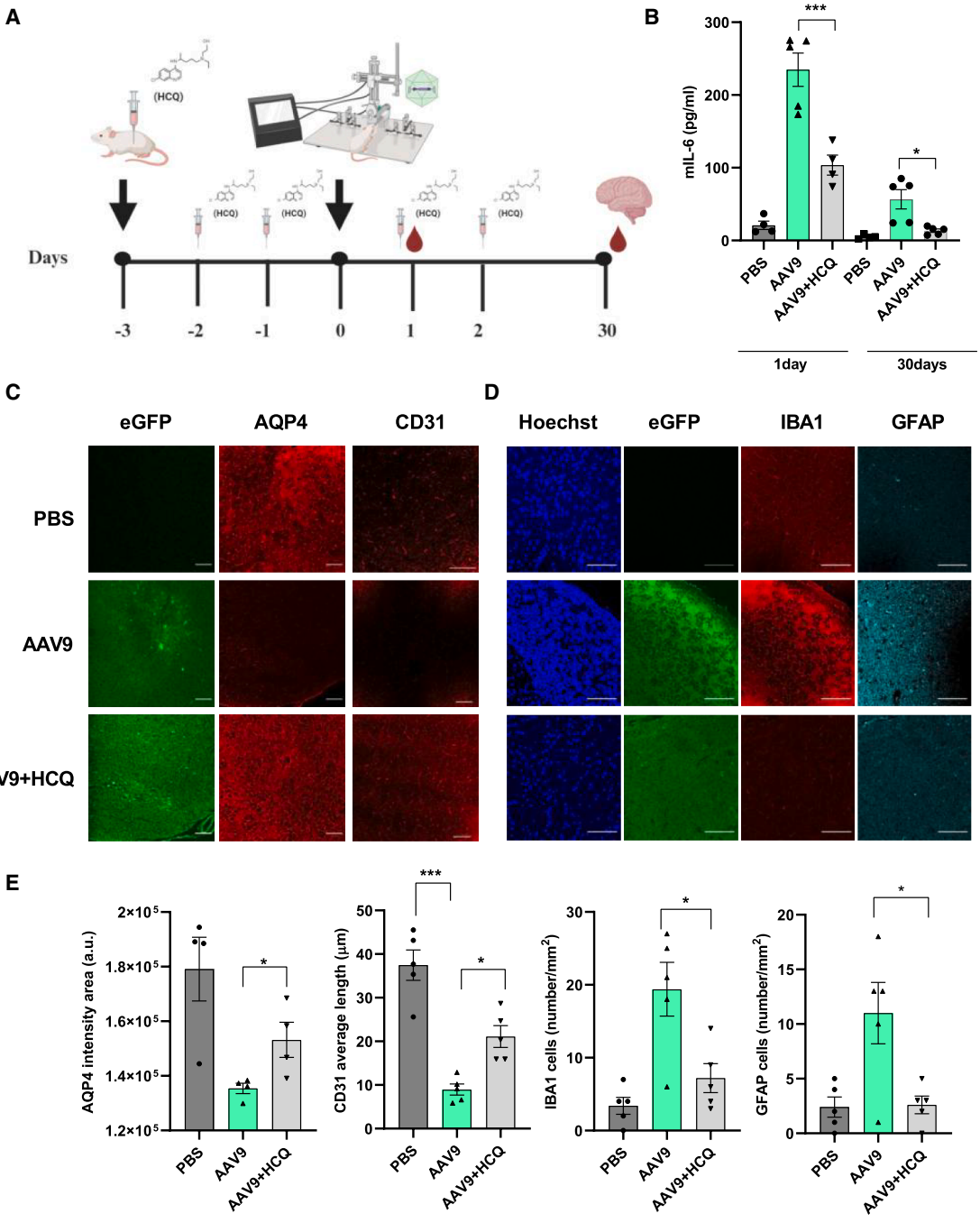


Figure 4. Selective early innate modulation reduces AAV9-induced blood-brain barrier damage while preserving transduction

Mice ($n = 5$) were given HCQ (60 mg/kg body weight) intraperitoneally for 3 consecutive days. Next, they were stereotactically injected into the right cortex with 1×10^{10} PFUs/animal of AAV9-EGFP. The animals were additionally treated with HCQ (60 mg/kg body weight) for the next 2 days. Blood was taken on the first and on the 30th day post-injection. On day 30, the experiment was terminated, and brains were harvested (A). ELISA measured mouse IL-6 cytokine in mouse sera. Each dot represents a value obtained from an individual animal ($n = 5$). *$p < 0.05$ and ***$p < 0.001$. All p values are from ordinary one-way ANOVA followed by Tukey's multiple comparisons test. Graphs present mean values ± SEM. (B). Immunohistochemistry (IHC) staining of mouse brain tissue sections of AQP4 and CD31 (C) and IBA1 and GFAP (D) with adjacent quantification graphs (E). Scale bars represent 100 μm. Representative images are shown. Each dot represents the average of measurements obtained from an individual animal ($n = 5$). *$p < 0.05$ and ***$p < 0.001$. All p values are from ordinary one-way ANOVA followed by Tukey's multiple comparisons test compared to blank. Graphs present mean values ± SEM.

Please cite this article in press as: Lainšček et al., Decoupling reactogenicity from efficacy enables safer mRNA vaccines, AAV gene delivery, and *in vivo* base editing, Molecular Therapy (2026), https://doi.org/10.1016/j.ymthe.2026.09.033

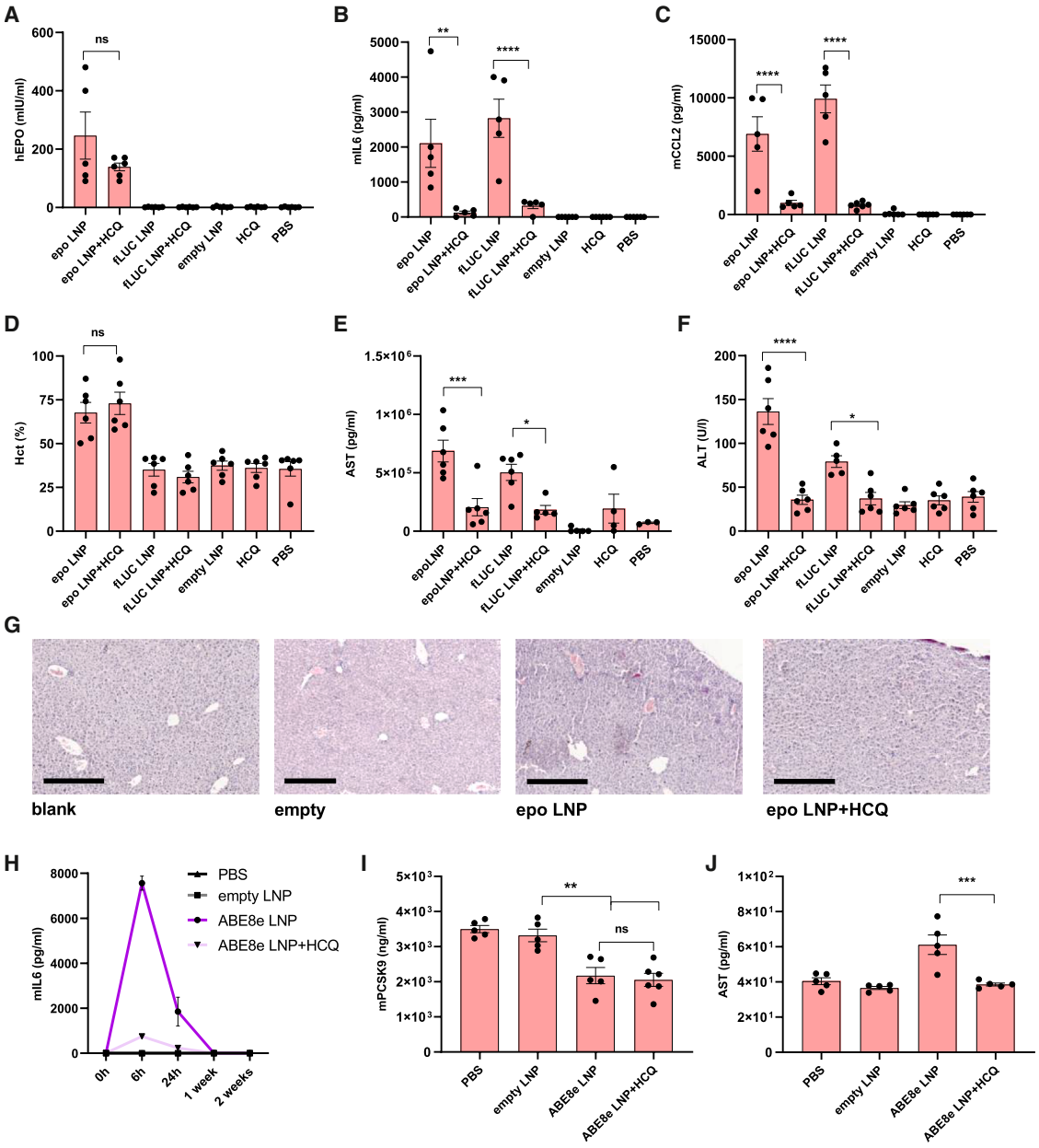


Figure 5. Early innate-sensing suppression mitigates LNP-mRNA hepatotoxicity and thrombocytopenia and supports base-editor dosing

(A–C) Erythropoietin (EPO) or fLUC mRNA/LNP (1 mg/kg; cap1/N1-mΨ mRNA) ± suppressor (HCQ, 60 mg/kg) applied every 72 h for 1 week. Human EPO (A), mouse IL-6 (B), and mouse CCL2 (C) at 6 h post-intravenous (i.v.) administration of LNPs, determined by ELISA. (D) Hematocrit on day 8. (E and F) ALT and AST on day 4. (G) Representative liver H&E sections (day 8). Scale: 300 μm. (H–J) ABE8e base editor + *Pcsk9* gRNA mRNA/LNP (1.5 mg/kg) ± suppressor (HCQ, 60 mg/kg) with re-dosing on day 3. Mouse IL-6 at 6 h (H), serum mouse PCSK9 on day 21 (I), and AST on day 4 (J). Each dot represents the average of measurements obtained from an individual animal (n = 5–6). *p < 0.05 and ***p < 0.001. All p values are from ordinary two-way ANOVA followed by Tukey's multiple comparisons test compared to blank. Graphs present mean values ± SEM.

effective therapeutic avenue. However, hepatotoxicity is a major barrier to clinical translation of high doses of LNP-delivered base editors, required for efficient editing. By delivering ABE8e mRNA with *Pcsk9* gRNA at a therapeutically relevant dose and setting, early cytokine induction was reduced, ALT/AST elevations were attenuated (Figures 5H–5J and S16), and serum Pcsk9 levels decreased as expected from on-target editing (Figure 5I). These data support selective early innate modulation as a generally applicable strategy to improve tolerability of repeated or higher-dose LNP-mRNA regimens, including genome editors.

Please cite this article in press as: Lainšček et al., Decoupling reactogenicity from efficacy enables safer mRNA vaccines, AAV gene delivery, and *in vivo* base editing, Molecular Therapy (2026), https://doi.org/10.1016/j.ymthe.2026.09.033

DISCUSSION

Here, we identify a conserved early innate inflammatory program, peaking at approximately 6 h after dosing, that follows NA delivery across mRNA/LNP, adenoviral, and AAV9 platforms. This transient program, dominated by pro-inflammatory cytokines and PRR-driven transcriptional signatures, represents a unifying biological response to therapeutic NAs. Importantly, we show that selective suppression of this early innate burst can be achieved without significantly impairing the downstream functional outcomes of vaccination or gene delivery: antibody titers, live-virus neutralization, $CD8^+$ cytotoxicity, transgene expression, and *in vivo* genome editing all remain intact. Although co-formulation of HCQ with BNT162b2 resulted in a modest reduction in live-virus neutralization, this effect was not observed when HCQ was administered prophylactically. While immediate co-delivery may attenuate the earliest innate signals contributing to optimal antibody priming, prophylactic administration sufficiently suppresses excessive inflammatory signaling without compromising functional immunity. Consistent with this, HCQ preserved a mature $MHCII^{high}CD38^{high}$ B cell phenotype and did not impair long-term humoral or cellular immune responses, as normal antibody values and a portion of CD44 were determined in a long-term *in vivo* study, further supporting our conclusion that HCQ selectively attenuates NA-induced inflammatory signaling rather than broadly suppressing immune function.

At the same time, key safety liabilities such as BBB disruption, liver enzyme elevations, and thrombocytopenia were substantially mitigated by the use of HCQ, thus presenting it as a suitable prophylactic in various therapeutic approaches.

Even when therapeutically delivered NAs are chemically identical to their endogenous counterparts,[16,25] aberrant localization (cytosolic DNA and endosomal RNA or DNA) renders them visible to innate surveillance. Before associating with endogenous RNA-binding proteins, these species can engage PRRs and trigger inflammatory cascades,[6,46] producing the characteristic early cytokine surge that precedes translation or vector uncoating.

Our findings support a model in which 4-aminoquinolines selectively attenuate NA-induced innate immune activation without compromising productive intracellular delivery or translation of therapeutic NAs. Previous studies have proposed that 4-aminoquinolines reduce the accessibility of NAs to endosomal PRRs, thereby limiting PRR engagement.[23,47] The small-molecule modulators tested in our study bind dsDNA and RNA species and reduce cytokine induction even after electroporation, indicating effects beyond endocytosis interference. Our data extend this model by demonstrating that these interactions are compatible with preserved mRNA translation. Protein expression remained unchanged following mRNA electroporation, LNP-mediated delivery, and cell-free translation, indicating that HCQ does not measurably interfere with productive cytosolic translation of delivered mRNA under the experimental conditions used in this study.

Although endosomal acidification is required for activation of endosomal NA-sensing pathways and contributes to LNP-mediated endosomal escape, HCQ-induced modulation of endosomal pH did not compromise transgene expression in our observations. Although endosomal acidification[48] is required for both activation of endosomal NA-sensing pathways and LNP-mediated endosomal escape, these processes occur over different pH ranges. Ionizable lipids used in clinically relevant LNPs possess apparent pKa values of approximately 6.1–6.7, enabling efficient protonation within the mildly acidic environment of early endosomes (approximately pH 6.0–6.5), where productive endosomal escape is thought to occur. In contrast, activation of endosomal TLRs depends on sustained acidification of late endosomes and lysosomes (approximately pH 4.5–5.5), where acidic proteases mediate receptor maturation and RNase-dependent ligand processing.[17,49] Indeed, measurements demonstrated only partial attenuation of endosomal acidification by HCQ, so we believe that the degree of pH modulation is sufficient to dampen endosomal NA sensing while remaining compatible with efficient cytosolic delivery of the mRNA cargo. In parallel, HCQ significantly reduced phosphorylation of NF-κB and IRF3, indicating attenuation of proximal signaling events downstream of NA recognition rather than nonspecific suppression of cellular function. Another study reported inhibition of p38 MAPK phosphorylation by HCQ after dsRNA stimulation,[50] indicating the effect of HCQ on the earlier inflammatory signaling pathway. Because NF-κB and IRF3 represent the major transcriptional regulators controlling expression of inflammatory cytokines and type I IFN-responsive genes downstream of NA sensing, these findings provide mechanistic evidence that HCQ acts upstream of innate signaling cascades. Transcriptomic profiling also revealed attenuation of TLR pathways while preserving IFNβ-associated response elements, offering a molecular explanation for reduced inflammation yet maintained vaccine priming. Together with the lack of effect on R848 and cGAMP, in agreement with other publications,[23,51] these data support a model in which HCQ prevents immunostimulatory NAs from efficiently engaging their cognate PRRs, thereby attenuating early activation of NF-κB and IRF3 and reducing downstream inflammatory cytokine production without broadly suppressing innate immune signaling.

This interpretation is further supported by our pathway-selective stimulation experiments. HCQ attenuated responses induced by NA-containing stimuli, whereas the response elicited by the small-molecule TLR7/8 agonist R848 and the STING agonist cGAMP remained largely preserved. Together, these findings demonstrate that HCQ does not act as a broad suppressor of innate immune signaling but instead selectively modulates pathways initiated by NA recognition. Accordingly, by inhibiting IL-6 and IFNγ secretion upon BNT162b2 stimulation of PBMCs, we discovered that CCL2 was diminished, suggesting that IL-6 and IFNγ act as key reactogenicity drivers. Combined with our transcriptomic analyses and preserved long-term humoral and cellular immune responses, these data support the central conclusion of this study: transient modulation of early NA sensing is sufficient to decouple innate reactogenicity

Please cite this article in press as: Lainšček et al., Decoupling reactogenicity from efficacy enables safer mRNA vaccines, AAV gene delivery, and *in vivo* base editing, Molecular Therapy (2026), https://doi.org/10.1016/j.ymthe.2026.09.033

from therapeutic efficacy while maintaining productive intracellular delivery and durable adaptive immunity.

Consistent with earlier reports,[49] we also confirmed that mRNA cargo is the principal driver of LNP reactogenicity, whereas the lipid components of LNPs alone are insufficient at comparable doses, consistent with the tolerability of empty LNPs. We observed an increase in liver enzymes to be mRNA/LNP-dose dependent and occurring only at clinically relevant doses, beyond 0.5 mg/kg. In the liver, suppression of the early innate program lowered ALT/AST elevations and rescued platelet counts, supporting the feasibility of repeat dosing and high-exposure regimens, which remain important bottlenecks for therapeutic mRNA and *in vivo* editing. In the CNS, where inflammation and vascular perturbations have disproportionate consequences, we observed reduced microgliosis and astrocytosis and preserved endothelial and perivascular integrity after AAV9 administration, pointing toward a route for safer intraparenchymal gene delivery.

Because the modulators used here are clinically established, orally bioavailable agents that associate with LNP cargo without altering particle size or encapsulation efficiency, this approach represents a practical and immediately accessible co-therapy. Unlike glucocorticoid co-therapy,[52] which globally dampens immune function, selective suppression of endosomal NA sensing preserves adaptive immunity while mitigating early toxicity. Optimization of dosing, timing, or co-formulation strategies may further enhance translational applicability. Together, these findings position endosomal NA-sensing suppressors, including but not limited to 4-aminoquinolines, as promising anti-reactogenic adjuncts capable of broadening the therapeutic window for mRNA medicines, viral vectors, and genome editing.

The study has certain limitations. All *in vivo* experiments were performed in mice, and translation to humans will require pharmacokinetic alignment and exposure matching, particularly for CNS delivery. We did not evaluate chronic multidose regimens beyond the tested schedules, although 4-aminoquinolines have a safety track record of long-term application for autoinflammatory conditions. Although adaptive immune priming was preserved in the settings tested, long-term cell and humoral immune responses were also researched and found to be unaffected. Some applications requiring strong adjuvanticity, such as therapeutic cancer vaccines, may not benefit from innate suppression.

Taken together, these results highlight that selective modulation of early innate sensing of NA therapeutics offers a practical and immediately accessible strategy to markedly improve the safety and flexibility of its use, with the potential to influence how next-generation mRNA vaccines, viral vectors, and *in vivo* genome-editing agents are designed and deployed.

MATERIALS AND METHODS

Cells

PBMCs for NA stimulation and electroporation were obtained from healthy donors. Samples were obtained with informed consent and according to the study protocol approved by the National Medical Ethics Committee (0120-199/2022/3) for conducting research to determine the immune response to COVID-19 vaccines. The cells were maintained in RPMI1640 (Invitrogen Life Technologies) cell medium, supplemented with 10% (v/v) heat-inactivated FBS (Invitrogen Life Technologies).

Mouse splenocytes for NA stimulation were obtained from spleens of different strains of mice, according to the EU 2010/63 directive. Tissue collection was approved by the Administration of the Republic of Slovenia for Food Safety, Veterinary Sector and Plant Protection of the Ministry of Agriculture, Forestry and Foods, Republic of Slovenia (permit number U34401-13/2022/3). Single-cell suspensions from spleens without enzymatic treatment were obtained using the tissue dissociator gentleMACSTM Dissociator, according to the manufacturer's instructions (Miltenyi Biotec, Bergisch Gladbach, Germany). Cells were maintained in RPMI1640 cell medium, supplemented with 10% (v/v) heat-inactivated FBS. The cells were treated with various NA-based vaccines in combination with HCQ. To determine cell death, an LDH cytotoxicity assay (Thermo Fisher Scientific) was carried out according to the manufacturer's protocol.

A549-dual cells (NF-κB-SEAP and IRF-Lucia reporter lung carcinoma) (Invivogen) were maintained in RPMI1640 cell medium, supplemented with 10% (v/v) heat-inactivated FBS. SEAP was determined using QUANTI-Blue - SEAP Detection Reagent (Invivogen) according to the manufacturer's protocol. rLUC was determined using a luminometer with coelentrazine buffers.

Cell electroporation

PBMCs (2×10^7 cells/mL) were electroporated using a Neon electroporation system (Thermo Fisher Scientific), using T buffer in 10 μL electroporation tips (electroporation parameters: 2,150 V, 20 ms pulse width, 1 pulse). The total amount of mRNA per electroporation was 1 μg.

Chemicals

Ionizable cationic aminolipid heptatriacont-6,9,28,31-tetraene-19-yl 4-(dimethylamino) butanoate (DLin-MC3-DMA; MC3, HY-112251), HCQ sulfate (HY-B1370), and Q dihydrochloride were purchased from MedChemExpress. 1,2-Diastearoyl-sn-glycero-3-phosphocholine (DSPC; SI-850365P) and cholesterol (Chol; C8667) were purchased from Sigma. 1,2-Dimyristoyl-glycero-3-methoxypolyethylene glycol-2000 (DMG-PEG2000; 880151P) was purchased from Avanti Lipids. CQ sulfate was purchased from Sigma. cGAMP (3′,3′) was purchased from MedChem Express. R848 and polyI:C were purchased from Invivogen. Human IL-6 (sc-28343) and human IFNγ (sc-373727) antibodies were purchased from Santa Cruz Biotechnology.

IVT mRNA synthesis

The mRNAs were prepared by *in vitro* transcription (IVT) with T7 RNA polymerase according to the manufacturer's instructions (Ribomax LargeScale RNA production System, Promega P1300) unless

Please cite this article in press as: Lainšček et al., Decoupling reactogenicity from efficacy enables safer mRNA vaccines, AAV gene delivery, and *in vivo* base editing, Molecular Therapy (2026), https://doi.org/10.1016/j.ymthe.2026.09.033

stated otherwise. We used purified PCR fragments for DNA templates, with an already encoded 102-bp-long poly(A) tail. dsRNA was synthesized using DNA templates with T7 promoters on both 3′ and 5′ ends. For integration of modified uracil nucleotides, Pseudo-UTP (Jena Bioscience NU-1139S) and N-methylpseudo-UTP (Jena Bioscience NU890-S), we added 20 μL of each, replacing non-modified UTP in the reaction mixture entirely. After DNase I treatment of the IVT reaction mix, we performed capping of mRNA using the Vaccinia capping system (NEB M2080S) for the formation of cap-0 and additionally cap 2-O'methyltransferase for the formation of cap-1 (NEB, NE-M0366S). mRNA was purified according to the manufacturer's instructions (Phenol-Chloroform extraction) or with NEB's Monarch RNA Cleanup Kit NEB T2040L. mRNA integrity and correct size were assessed using Agilent's 2100 Bioanalyzer with the Agilent RNA 6000 Pico kit (5067-1513 and 5067-1514); concentration and A260/A280 ratios were measured on a Nanodrop.

LNP formulation and characterization

LNPs encapsulating mRNA were prepared as previously reported,[53] using the Precision Nanosystems Ignite microfluidic mixing platform. Briefly, we first prepared a lipid formulation in ethanol at molar ratios of 50.5:10:38:1.5 (MC3/DSPC/Chol/DMG-PEG2000). Thus, a prepared lipid mix with a final lipid concentration of 12.5 mM and mRNA concentration of 0.174–0.200 mg/mL in 25 mM citrate buffer (pH 4.0) was injected into the NxGen cartridge at a flow rate ratio of 1:3 with a final flow rate of 12 mL/min. The N/P ratio was 4 (cationic ionizable lipid to anionic mRNA). Subsequently, we diluted the product 10 times in phosphate-buffered saline (PBS; pH 7.4) and concentrated the diluted product at 2,000*g* for 30 min. LNPs were filtered through 0.22 μM membranes and stored at 4°C or −80°C (diluted 2× with 10% sucrose solution). BNT162b2 mRNA/LNP and chimp-adenoviral vector AZD1222 doses against the SARS-CoV-2 ancestral strain that remained unused were used, based on the approval of the Medical Ethics Board of Slovenia and local authorities at Regierung Oberbayern, Munich, Germany.

The size and distribution of in-house-made LNPs and BNT162b2 vaccine were characterized with dynamic light scattering (measured using a Malvern Zetasizer). mRNA encapsulation efficiency and concentration inside LNPs were determined using the QuantiTRibogreen RNA assay (Molecular Probes R-1141) and Quantifluor RNA system (Promega E3310).

Fluorescence spectroscopy

HCQ (1 mM) was mixed with various concentrations of NAs, LNPs, or vaccines (AZD1222 and BNT162b2) at room temperature in a 96-well black microplate. In the competition assay, the PI (50 μM) was added to the mixture. Fluorescence measurements were performed with a microplate reader (BioTek) using excitation at 330 nm for HCQ and excitation at 535 nm for PI. The emission spectra of HCQ and PI were recorded between 450 and 580 or 550 and 750 nm, respectively. All compounds were dissolved in Milli-Q.

RNA-seq

Total RNA was extracted from homogenized lymph node and muscle tissue using TriPure Isolation Reagent (Merck) and High Pure RNA Isolation Kit (Roche) following manufacturers' instructions. Purity (ratios A260/280 and A260/230) and quantity were measured on a Nanodrop spectrometer (Thermo Fisher Scientific). Three biological repeats of each sample were sent for sequencing at Azenta Life Sciences (Genewiz, Leipzig). They performed sample quality control (QC), library preparation, rRNA removal by poly(A) selection for mRNA species from muscle tissue, and rRNA depletion for lymph nodes due to lower-quality RNA samples. The libraries were run on Illumina NovaSeq, using the 2 × 150 bp paired-end sequencing protocol, with a sequencing depth of 20–30 million reads per sample. First, we performed QC with FastQCheck, then paired-end adapter trimming, using CutAdapt.[54] Then, we "pseudo-aligned" trimmed samples to the mouse genome, using Kallisto pseudo-alignment[55] with pre-produced index and GFT files, downloaded from the Kallisto transcriptome indices data source (version June 22, 2019; Kallisto 0.45.1, Ensembl v.96 transcriptomes). Differential expression was performed using RStudio (RStudio 4.3.2 [2023-10-31 ucrt]) with the R package DESeq2.[56] Data were normalized with the built-in function median of ratios, and threshold of significance was set to adjusted p (adj. p) < 0.05. Volcano plots were drawn with the EnhancedVolcano[57] Bioconductor package. To perform enrichment analysis, we took significantly upregulated genes of each sample (adj. $p < 0.05$, $\log_2$ fold change [$\log_2$FC] > 0) as an input to the web-based gene set analysis toolkit (WebGestalt).[58] We performed ORA (over-representation analysis), and for annotation, we chose the functional database Gene Ontology (non-redundant biological process). The data were submitted to the GEO repository (GEO: GSE277440).

In vitro translation assay

Translation efficiency was assessed using the rabbit reticulocyte lysate system (Promega L4960). Briefly, reaction mixtures were prepared according to the manufacturer's protocol and incubated at 30°C for 90 min. The reaction mixtures were diluted 10× in PBS buffer, and enzymatic activity was measured using a microplate luminometer (Berthold).

ELISAs

Values of human IL-6 and IFNγ were determined using the Human IL6 ELISA Kit (Invitrogen) and Human IFNγ (eBioscience) according to the manufacturer's protocol. Mouse IL-6, CCL2, IL-2, and IFNγ were determined by the IFN gamma ELISPOT ELISA Ready-SET-Go! Kit (15531137, eBioscience, San Diego, CA, USA) according to the manufacturer's protocol. Human EPO values were determined using the Human EPO ELISA kit (Thermo Fisher Scientific) following the manufacturer's instructions. Human IL-10 (Invitrogen), human CCL2 (Thermo Fisher Scientific), human TNFα (eBioscience), human IL-8 (eBioscience), and human IL1β (Invitrogen) were determined according to the manufacturer's protocol.

Please cite this article in press as: Lainšček et al., Decoupling reactogenicity from efficacy enables safer mRNA vaccines, AAV gene delivery, and *in vivo* base editing, Molecular Therapy (2026), https://doi.org/10.1016/j.ymthe.2026.09.033

pH endosome modulation measurements

HEK293 cells were seeded in 8-well chamber slides (Ibidi, Germany) at a density of 5×10^5 cells/mL. 24 h later, HCQ (5 μM) was added. Both HCQ-treated and untreated control cells were included in the experiment. Cells were incubated for 10–12 h with a mixture of 10 kDa dextran-FITC (0.5 mg/mL) and 10 kDa dextran-AF647 (0.1 mg/mL), applied in either the presence or absence of HCQ. In addition, cells stained with each dextran individually were used as single-color controls to assess fluorescence bleed-through between imaging channels. Confocal fluorescence imaging was performed using a Leica TCS SP8 confocal microscope equipped with a 63× oil-immersion objective. FITC fluorescence was excited using a 488 nm laser line and detected between 510 and 540 nm, while AF647 fluorescence was excited using a 633 nm laser line and detected between 645 and 680 nm. At least 10 single-plane images from independent microscopic fields were acquired for each experimental condition using identical acquisition settings. The presented data represent a single biological replicate. For quantitative image analysis, all images were converted to 8-bit grayscale format using ImageJ/Fiji software (ImageJ 1.54p; Java 1.8.0_322). The AF647 channel was used to segment endosomal/lysosomal structures due to its pH-independent fluorescence signal. Briefly, AF647 images were processed using the "Smooth" function to reduce pixel-level noise, followed by thresholding to remove background fluorescence and generate binary masks corresponding to vesicular structures. These masks were subsequently used to define ROIs representing endosomal and lysosomal compartments. The generated ROI sets were transferred onto the original, unprocessed AF647 and FITC images. Mean fluorescence intensity was measured for each ROI in both channels. To compensate for variability in dextran uptake and vesicle content, FITC fluorescence intensity was normalized to the corresponding AF647 fluorescence intensity for each ROI. The normalized FITC/AF647 fluorescence ratio was used as a quantitative indicator of endosomal pH. All ROIs from all acquired images were included in the calculation of experimental averages.

Bio-plex analysis

Multiplexing of mouse cytokines and chemokines was determined by using Bio-Plex Pro Mouse Cytokine Grp I panel 23-plex (Bio-Rad) according to the manufacturer's instructions. For readouts, the Bio-Plex 200 System was used with Bio-Plex Manager, v.6.2 (Bio-Rad).

Phosphorylation status of NF-κB and IRF3

PBMCs (10^6) were stimulated with BNT162b2 (2 μg) in the presence of HCQ (5 μM). Cells were lysed with 5xPassive Lysis buffer (Promega) and left on ice for 30 min. After that, the lysates were centrifuged for 30 min at 13,400 rpm. Total protein quantification was carried out using the QuantiPro BCA Assay Kit (Sigma). Proteins (75 μg) were separated by SDS-PAGE and transferred to a Hybond ECL nitrocellulose membrane (GE Healthcare). Blots were incubated with appropriate antibodies. Primary antibodies used for western blotting were as follows: beta-Actin (13E5) Rabbit Monoclonal Antibody (Cell Signaling, 4970), Phospho-NF-kappaB p65 (Ser536) (93H1) Rabbit Monoclonal Antibody (Cell Signaling, 3033), NF-κB p65 (D14E12) Rabbit Monoclonal Antibody (Cell Signaling, 8242), Phospho-IRF-3 (Ser396) (D6O1M) Rabbit Monoclonal Antibody (Cell Signaling, 29047), and IRF-3 (D83B9) Rabbit Monoclonal Antibody (Cell Signaling, 4302). Secondary antibodies used for western blotting were goat polyclonal anti-rabbit IgG (ab6721) from Abcam. The immunoblots were visualized on a G-box (Syngene) after chemiluminescence detection using Pierce Fast Western Blot Kits, SuperSignal West Femto (Thermo Fisher Scientific), according to the manufacturer's instructions. To determine the level of phosphorylation status of NF-κB and IRF3, band quantification was performed using ImageJ. Band intensities of pNF-κB or pIRF3 and total NF-κB or IRF3 were first normalized to β-actin. Relative NF-κB phosphorylation or IRF3 was then calculated as the ratio between β-actin-normalized pNF-κB or pIRF3 and β-actin-normalized total NF-κB or total IRF3 and expressed relative to the control group.

Spectral flow cytometry analysis

Cells ($4–5 \times 10^6$) were resuspended in FACS buffer (150 μL, PBS supplemented with 10% FBS). For live/dead staining, ZombieNIR dye was used according to the manufacturer's protocol. Briefly, the fluorescence-activated cell sorting (FACS) buffer was replaced with 100 μL PBS containing ZombieNIR dye (dilution 2,000 to 5,000). Samples were incubated for 10–15 min on ice, and the reaction was stopped with the addition of FACS buffer (100 μL). The ZombieNIR dye was removed with centrifugation at 450 rpm, and the collected cells were resuspended in 50 μL FACS buffer containing 2 μL Mouse TrueSatin FcX (BioLegend) or anti-mouse CD16/CD32 (Fcy III/II receptor) (BD Pharmingen). Ten minutes later, an antibody cocktail was added (50 μL) to the mixture, and samples were incubated for at least 30 min on ice. The antibody cocktail was prepared in FACS buffer containing 5 μL True Stain Monocyte blocker (426103, BioLegend). See Table S1 for a list of the antibodies used in this study. Before analysis, cells were washed with FACS buffer, and fluorescence was measured on the 3-laser Aurora spectral flow cytometer (Cytek Bioscience). All antibodies were titrated individually according to standard practice before being used in the panel. As reference controls, an unstained sample and, for every color, a single-stain reference control were acquired. All reference controls underwent the same protocol as fully stained samples, including washes. Reference controls were acquired once and used to unmix multiple batches. For all parameters, a cell type of interest was used. Data were acquired and unmixed using SpectroFlo v.3.1.0 software (Cytek Bioscience) using the same instrument settings for every run. The resulting unmixed fetal calf serum (FCS) files were analyzed using manual gating in Flowood software (BD Biosciences). First, a manual data check was performed to ensure the exclusion of technical artifacts and bad-quality samples (clogs, doublets, and dead cells). The unmixing of raw data was performed using single-stain controls as references (no manual compensation was used). FlowAI software was used to exclude noise, anomalies in flow rate, signal acquisition, and outlier events.[59] Next, doublets and dead cells were removed, and CD45-positive cells were gated manually, subsampled using the FlowJo_Downsample function, and saved as

new FCS 3.1 files. Before dimensionality reduction and clustering, the new files were merged using the FlowJo_Concatenation function. The manually gated cells were further analyzed using the uniform manifold approximation and projection (UMAP) dimensionality reduction method and X-shift/FlowSOM clustering approach. For T cell dimensionality reduction, CD4, CD8, MHCII, CD103, CD11b, CD86, CD69, CD62L*, and CD44* markers were used; for B cells, MHCII, CD62L*, CD44*, CD86, CD161, and CD11c were used; and for the rest of the cells, CD103, CD44*, CD4, CD62L*, CD11c, MHCII, CD11b, CD8a, CD64, Ly6C, CD86, and CD69 were used. FCS files are available upon request.

Mouse studies

All animal experiments were performed according to the directives of the EU 2010/63 and were approved by the Administration of the Republic of Slovenia for Food Safety, Veterinary Sector and Plant Protection of the Ministry of Agriculture, Forestry and Foods, Republic of Slovenia (permit numbers U34401-9/2022/4, U34401-6/2025/8, and U34401-11/2025/8). Laboratory animals were housed in IVC GM500 cages (Techniplast) and fed standard chow (Mucedola), and tap water was provided *ad libitum*. The cages were enriched using Nestlets nesting material and mouse houses. Mice were maintained in a 12-h/12-h dark-light cycle at approximately 40%–60% relative humidity with 22°C of ambient temperature. All animals used in the study were healthy, accompanied by a health certificate from the animal vendor. Health/microbiological status was confirmed by the FELASA-recommended Mouse Vivum immunocompetent panel (QM Diagnostics).

To test the effect of HCQ on NA immunizations, female 8- to 10-week-old C57BL/6J OlaHsd mice were used. Mice were intramuscularly immunized with COVID-19 vaccine (BNT162b2 [Pfizer], 4 μg/animal; AZD1222 [AstraZeneca], 3.5×10^4 plaque-forming units [PFUs]/animal; or in-house-prepared LNPs, containing spike mRNA); 4 μg/animal, expressing the spike protein of interest, combined with HCQ sulfate (60 mg/kg of body weight of the animal), combined into a single injectable composition if not stated otherwise. COVID-19 vaccines were technical waste obtained from Golnik Hospital or from TUM. In some cases, HCQ was administered 24 h before the vaccine. Immunization was carried out under general inhalation 1.8% MAK isoflurane anesthesia (Harvard Apparatus). Vaccine (prime; first dose) was administered using a 30G needle into *m. tibialis anterior* after appropriate area preparation. The boost (second dose) was administered 3 weeks later. Blood was drawn 6 and 24 h after the prime. Blood was taken again before the first boost and again 6 and 24 h after the first boost. Blood was drawn from the lateral tail vein using Microvette 300 (Sarstedt). Three weeks after the boost, the experiment was terminated unless stated otherwise. Final blood was taken, and spleens were harvested from animals. Mouse sera were prepared by centrifugation of blood samples at 3,000 rpm/20 min at 4°C.

To study the effect of LNP-induced liver damage and thrombocytopenia, a mixture of HCQ (60 mg/kg) and LNPs containing *in-vitro*-transcribed human EPO mRNA (cap-1 N1-mΨ) or fLUC mRNA or EGFP was injected intravenously in C57BL/6J OlaHsd (female mice, aged 8–10 weeks) every 72 h for 1 week. Blood was taken at 6 h post-first injection and then on day 8.

A complete biochemical profile was determined using the VetScan Mammalian Liver Profile reagent and the Comprehensive Metabolic Panel rotor and analyzed on the VetScan VS2 biochemistry analyzer (Abaxis). Five-part complete blood count was performed using the VetScanHM5 Hematology Analyzer (Abaxis).

Mouse *Pcsk9 in vivo* base editing

LNPs, containing ABE8e mRNA (cap-1 N1-mΨ) and gRNA (CCCATACCTTGGAGCAACGG,[41] purchased from Synthego), which was *in vitro* transcribed using mMESSAGE mMACHINE T7 mRNA Kit with CleanCap Reagent AG (Thermo Fisher Scientific), were injected into BALB/c OlaHsd female mice, aged 6 weeks, at a dose of 1.5 mg/kg of body weight, followed by another dose 3 days later. Blood was taken to evaluate cytokines, liver enzymes, and mouse PCSK9 levels using ELISA (Sinobiological). Three weeks later, organs were harvested, and pathohistological analysis was performed. After 48 h of fixation in 10% neutral buffered formalin (Sigma-Aldrich) and gradient ethanol dehydration, the tumor samples were embedded in paraffin (Leica Biosystems), sectioned into 7 μm pieces using a microtome (Leica Biosystems), and mounted on adhesive-coated slides (Leica Microsystems). After deparaffinization and hydration, sections were stained with Mayer's Hematoxylin Solution (Merck) and Eosin Y solution (Sigma-Aldrich). Histology slides were scanned using Ocus40 (Grundium), and pictures were analyzed using Aperio ImageScope v.12.4.6.5003 (Leica).

Inducing BBB damage

To induce BBB damage, 10-week-old female C57BL/6J OlaHsd mice were used. By stereotactic injection, performed as described in Guo et al.[20] AAV9-GFP (Origene) was injected into the right cortex (AP [anterior-posterior] +0.6 mm, ML [medial-lateral] −2 mm, DV [dorsal-ventral] −0.7 mm) using the 71000 Automated Stereotaxic Instrument (RWD). Each animal was injected with 1×10^{10} PFUs of AAV viruses in a total volume of 1.5 μL. The next day and on day 30, blood was taken to check for mouse IL-6 values. On day 30, EGFP fluorescence was determined using the spectral unmixing mode *in vivo* imaging system IVISIII (PerkinElmer, Waltham, MA, USA). Fluorescence values are presented as average radiant efficiency ($p/s/cm^2/sr$; $\mu W/cm^2$), which were determined using Living Image software. The animals were humanely sacrificed on day 30, the brains were removed, snap-frozen in liquid nitrogen, and used for further immunohistochemistry analysis. Using a cryostat MEV (SLEE Medical), 6 μm brain tissue slices were cut. Cell nuclei were stained with Hoechst dye (Invitrogen). For GFAP detection, mouse GFAP (GA5) (Cell Signaling Technology; dilution 1:100) antibody was used. AF568 goat anti-mouse IgG (H+L) 2 mg/mL (Invitrogen; dilution 1:1,000) was used as a secondary antibody. For CD31 quantification, rat CD31/PECAM-1 antibody was used (Santa Cruz Biotechnology; dilution 1:50), whereas rabbit IBA1/AIF-1 (E4O4W) XP (Cell

Please cite this article in press as: Lainšček et al., Decoupling reactogenicity from efficacy enables safer mRNA vaccines, AAV gene delivery, and *in vivo* base editing, Molecular Therapy (2026), https://doi.org/10.1016/j.ymthe.2026.09.033

Signaling Technology; dilution 1:1,000) was used for IBA1 detection. AQP4 was stained with rabbit AQP4 (D1F8E) XP antibody (Cell Signaling Technology; dilution 1:200), and the NeuN marker was determined by rabbit NEUN (D4G4O) XP antibody (Cell Signaling Technology; dilution 1:400). AF647 F(ab)2 fragment of goat anti-rabbit IgG (H+L) 2 mg/mL (Invitrogen; dilution 1:1,000) were used as secondary antibodies for CD31, IBA1, AQP4, and NeuN. Images were acquired using a Leica TCS SP5 inverted laser-scanning microscope on a Leica DMI 6000 CS module (Leica Microsystems) equipped with an HCX Plane-Apochromat lambda blue 63× oil-immersion objective with numerical aperture 1.4. Quantification of images was done using LasX software (Leica).

Analysis of immune response in mice

In mouse sera, specific anti-spike SARS-CoV-2 total IgG was determined by ELISA to test the immunogenicity of vaccines and determine the effect of HCQ on antibody production. ELISA tests were performed to determine the EPT. High-binding half-well plates (Greiner) were used. To determine specific anti-spike SARS-CoV-2 total IgG, recombinant His-spike SARS-CoV-2 protein (prepared in-house as described elsewhere[60]) was used for coating of the ELISA plates. Recombinant proteins were coated in PBS buffer at a concentration of 50 ng of designed protein per well. The total volume of the coated solution was 50 μL/well. Coated plates were incubated overnight at 4°C. The next day, plates were washed with PBS+0.05% Tween 20 using an ELISA plate washer (Tecan). Next, plates were blocked for 1 h at RT with ELISA diluent (PBS+3%FBS) solution. Afterward, the plates were again washed. Then, a serial dilution (factor of 10) of mouse sera was added to the plates, where each dilution presented a certain titer value. For mouse sera, ELISA diluent was used. Mouse sera were incubated at 4°C overnight. The next day, plates were washed, and then goat anti-mouse IgG (H+L)-HRP antibodies (Jackson ImmunoResearch) were diluted 1:3,000 in ELISA diluent solution. Plates were incubated for 1 h at RT. Next, plates were washed. After the final wash, TMB substrate was added, and the reaction was stopped with the addition of acid solution (3M H_3PO_4). Absorbance (A450 nm and A620 nm) was measured by Synergy Mx microtiter plate reader (Biotek). Next, EPTs were calculated. The EPT was determined as the dilution above the value of the cutoff.

From absorbance data of control animals (non-treated animals), the cutoff value was determined.[61] For a confidence level of 95%, a value of 2,335 was used as the standard deviation multiplier.

T cell response on mouse splenocytes

To determine antigen-specific cytotoxic $CD8a^+$ T cells, spleens from immunized mice were harvested. Single-cell suspensions from spleens without enzymatic treatment were obtained using the tissue dissociator gentleMACSTM Dissociator, according to the manufacturer's instructions (Miltenyi Biotec). $CD8^+$ T cells from spleen cell suspension were isolated using the mouse $CD8a^+$ T cell Isolation Kit (Miltenyi Biotec; 130-104-075), according to the manufacturer's instructions. Cells were isolated based on negative selection using LS columns (Miltenyi Biotec), yielding up to 10^8 labeled cells. To determine SARS-CoV-2 spike-specific cytotoxicity, NIH 3T3 mouse cells were seeded into 24-well plates (10^5/well); the next day, the cells were transfected with pCG1-hACE2 (900 ng/well) and pCMV-TMPRSS2 (30 ng/well) plasmids. The following day, cells were infected with spike pseudovirus with a bioluminescent reporter (prepared in-house as described elsewhere).[55] The day after, isolated $CD8a^+$ T cells (10^5/well) in RPMI1640 cell medium were added. After 24 h, bioluminescence was determined using IVISIII (PerkinElmer) following the addition of D-luciferin (500 μM), indicating the state of spike-specific cytotoxicity of the $CD8^+$ T cells isolated from vaccinated animals. Bioluminescence values are presented as average radiance (p/s/cm^2/sr), which were determined using Living Image software. From the average radiance values (ARVs), the percentage of infected NIH 3T3-specific lysis was calculated using the following formula: % specific lysis = 100 × (spontaneous death ARV − test ARV)/(spontaneous death ARV − maximal killing ARV). From the supernatants, mouse IL-2 and mouse IFNγ levels were determined.

Viral strains

SARS-CoV-2 EU1 strain (EPI_ISL_582134) was isolated from a nasopharyngeal swab of a patient during the first COVID-19 wave in March 2020. The virus was further propagated in Vero E6 cells (ATCC-CRL-1586) cultured in DMEM supplemented with 10% FCS, 1% penicillin/streptomycin, 200 mmol/L L-glutamine, 1% MEM-non-essential amino acids, and 1% sodium pyruvate (all from Gibco, Thermo Fisher). A plaque assay was applied to determine the virus titer in PFUs.

Infection neutralization assay

Vero E6 cells were seeded at 1.5×10^4 cells/well in a 96-well plate supplemented with DMEM medium and incubated overnight at 37°C and 5% CO_2. Serum samples were diluted 1:25 in culture medium, followed by a 5-fold serial dilution. Serum dilutions were mixed with SARS-CoV-2 virus to reach a multiplicity of infection (MOI) of 0.03 (450 PFUs/15,000 cells/well) and incubated at 37°C for 1 h to enable virus neutralization. The inoculum was then incubated on Vero E6 cells for 1 h at 37°C. Afterward, the sample/virus mix was replaced with medium, and cells were cultured for 24 h. As a positive control, cells were infected with the same MOI of the virus without incubation with serum samples, whereas uninfected Vero E6 cells represent the mock. To stop the infection, the cells were rinsed once with PBS and fixed with 4% paraformaldehyde (ChemCruz) at RT for 15 min. After an additional PBS wash, fixed Vero E6 cells were permeabilized for 15 min at room temperature with 0.5% saponin (Roth) in PBS and blocked with PBS with 0.1% saponin and 10% BSA (Roth) overnight at 4°C. The next day, VeroE6 cells were incubated for 2 h at room temperature with a 1:1,500 dilution of SARS-CoV-2 nucleocapsid antibody T62 (Sino Biological, Cat. No. 40143-T62) in PBS supplemented with 1% FCS. Cells were rinsed with wash buffer (PBS supplemented with 0.05% Tween 20 [Roth]) and incubated for 1 h at room temperature with goat anti-rabbit IgG antibody, HRP conjugate (Merck KGaA, Cat. No. 12-348), and 1:4,000 diluted in PBS/1% FCS. After thorough

washing, 100 μL TMB substrate (Invitrogen) was applied to each well and incubated at RT for 8 min in the dark. The reaction was stopped by adding 50 μL of 2 N H_2SO_4 (Roth), and colorimetric detection was performed on an Infinite F200 multi-plate reader (Tecan Group AG) at 450 and 560 nm. The data were fitted to a log(inhibitor) vs. response model with a variable slope in Prism v.8 (GraphPad).

Statistical analyses

Data are presented as means ± SEM. One-way ANOVA followed by Tukey's multiple comparisons test was used for the statistical comparison of data, unless stated otherwise. $^{*}p < 0.05$, $^{**}p < 0.01$, $^{***}p < 0.001$, and $^{****}p < 0.0001$. Graphs were prepared using GraphPad Prism8.

DATA AND CODE AVAILABILITY

All data supporting the findings are available within the paper and supplemental information. RNA-seq data are deposited in GEO under accession GEO: GSE277440. Raw flow cytometry FCS files and source data for graphs are available from the corresponding author upon reasonable request. Custom analysis used standard tools (Cutadapt, Kallisto, DESeq2, EnhancedVolcano, and WebGestalt); analysis scripts are available upon reasonable request.

ACKNOWLEDGMENTS

We thank K. Podgoršek for animal facility support and C.-C. Cheng for neutralization assay setup. Figures were created with BioRender.com. This work was funded by Slovenian Research Agency grants (P4-0176, GC-0005 and J4-4563 to R.J. and J4-4563 to D.L.), EU HorizonTeaming grant 101059842 (R.J.), EU H2020 FET Open VIROFIGHT grant 899619 (U.P. and R.J.), and BMBF C-NATM grant 03ZU1201BA (U.P.).

AUTHOR CONTRIBUTIONS

Conceptualization, D.L., Š.M., and R.J.; methodology, D.L., Š.M., R.J., A.G.-U., and U.P.; investigation, D.L., Š.M., J.B., A.G.-U., S.O., T.S., M.B., H.E., J.P.-Ž., M.M.K., V.F., P.P., and R.B.; visualization, D.L. and M.B.; funding acquisition, R.J., U.P., and D.L.; project administration, R.J. and U.P.; supervision, R.J.; writing – original draft, D.L., Š.M., and R.J.; writing – review & editing, D.L., Š.M., U.P., P.P., and R.J.

DECLARATION OF INTERESTS

R.J., D.L., Š.M., and A.G.-U. are inventors on a patent application related to this work.

DECLARATION OF GENERATIVE AI AND AI-ASSISTED TECHNOLOGIES IN THE MANUSCRIPT PREPARATION PROCESS

During the preparation of this work, the authors used ChatGPT solely for grammar polishing. After using this tool/service, the authors reviewed and edited the content as needed and take full responsibility for the content of the publication.

SUPPLEMENTAL INFORMATION

Supplemental information can be found online at https://doi.org/10.1016/j.ymthe.2026.09.033.

REFERENCES

1. Neufeld, E.F., Sweeley, C.C., Rogers, S., Friedmann, T., and Roblin, R. (1972). Gene therapy for human genetic disease? Science *178*, 648–649. https://doi.org/10.1126/science.178.4061.648.

2. Egli, M., and Manoharan, M. (2023). Chemistry, structure and function of approved oligonucleotide therapeutics. Nucleic Acids Res. *51*, 2529–2573. https://doi.org/10.1093/nar/gkad067.

3. Curreri, A., Sankholkar, D., Mitragotri, S., and Zhao, Z. (2023). RNA therapeutics in the clinic. Bioeng. Transl. Med. *8*, e10374. https://doi.org/10.1002/btm2.10374.

4. Cetin, B., Erendor, F., Eksi, Y.E., Sanlioglu, A.D., and Sanlioglu, S. (2025). Advancing CRISPR genome editing into gene therapy clinical trials: progress and future prospects. Expert Rev. Mol. Med. *27*, e16. https://doi.org/10.1017/erm.2025.10.

5. Sahin, U., Muik, A., Derhovanessian, E., Vogler, I., Kranz, L.M., Vormehr, M., Baum, A., Pascal, K., Quandt, J., Maurus, D., et al. (2020). COVID-19 vaccine BNT162b1 elicits human antibody and TH1 T cell responses. Nature *586*, 594–599. https://doi.org/10.1038/s41586-020-2814-7.

6. Li, C., Lee, A., Grigoryan, L., Arunachalam, P.S., Scott, M.K.D., Trisal, M., Wimmers, F., Sanyal, M., Weidenbacher, P.A., Feng, Y., et al. (2022). Mechanisms of innate and adaptive immunity to the Pfizer-BioNTech BNT162b2 vaccine. Nat. Immunol. *23*, 543–555. https://doi.org/10.1038/s41590-022-01163-9.

7. Maelfait, J., Liverpool, L., and Rehwinkel, J. (2020). Nucleic Acid Sensors and Programmed Cell Death. J. Mol. Biol. *432*, 552–568. https://doi.org/10.1016/j.jmb.2019.11.016.

8. Vanpouille-Box, C., Hoffmann, J.A., and Galluzzi, L. (2019). Pharmacological modulation of nucleic acid sensors — therapeutic potential and persisting obstacles. Nat. Rev. Drug Discov. *18*, 845–867. https://doi.org/10.1038/s41573-019-0043-2.

9. Crossley, M.P., Song, C., Bocek, M.J., Choi, J.H., Kousouros, J.N., Sathirachinda, A., Lin, C., Brickner, J.R., Bai, G., Lans, H., et al. (2023). R-loop-derived cytoplasmic RNA–DNA hybrids activate an immune response. Nature *613*, 187–194. https://doi.org/10.1038/s41586-022-05545-9.

10. Gaidt, M.M., Ebert, T.S., Chauhan, D., Ramshorn, K., Pinci, F., Zuber, S., O'Duill, F., Schmid-Burgk, J.L., Hoss, F., Buhmann, R., et al. (2017). The DNA Inflammasome in Human Myeloid Cells Is Initiated by a STING-Cell Death Program Upstream of NLRP3. Cell *171*, 1110–1124.e18. https://doi.org/10.1016/j.cell.2017.09.039.

11. Au, L., Fendler, A., Shepherd, S.T.C., Rzeniewicz, K., Cerrone, M., Byrne, F., Carlyle, E., Edmonds, K., Del Rosario, L., Shon, J., et al. (2021). Cytokine release syndrome in a patient with colorectal cancer after vaccination with BNT162b2. Nat. Med. *27*, 1362–1366. https://doi.org/10.1038/s41591-021-01387-6.

12. Felten, R., Kawka, L., Dubois, M., Ugarte-Gil, M.F., Fuentes-Silva, Y., Piga, M., and Arnaud, L. (2021). Tolerance of COVID-19 vaccination in patients with systemic lupus erythematosus: the international VACOLUP study. Lancet Rheumatol. *3*, e613–e615. https://doi.org/10.1016/S2665-9913(21)00221-6.

13. Tang, W., Gartshteyn, Y., Ricker, E., Inzerillo, S., Murray, S., Khalili, L., and Askanase, A. (2021). The Use of COVID-19 Vaccines in Patients with SLE. Curr. Rheumatol. Rep. *23*, 79. https://doi.org/10.1007/s11926-021-01046-2.

14. Stampfer, S.D., Goldwater, M.S., Jew, S., Bujarski, S., Regidor, B., Daniely, D., Chen, H., Xu, N., Li, M., Green, T., et al. (2021). Response to mRNA vaccination for COVID-19 among patients with multiple myeloma. Leukemia *35*, 3534–3541. https://doi.org/10.1038/s41375-021-01354-7.

15. Linares-Fernández, S., Lacroix, C., Exposito, J.Y., and Verrier, B. (2020). Tailoring mRNA Vaccine to Balance Innate/Adaptive Immune Response. Trends Mol. Med. *26*, 311–323. https://doi.org/10.1016/j.molmed.2019.10.002.

16. Zhang, H., Zhang, L., Lin, A., Xu, C., Li, Z., Liu, K., Liu, B., Ma, X., Zhao, F., Jiang, H., et al. (2023). Algorithm for optimized mRNA design improves stability and immunogenicity. Nature *621*, 396–403. https://doi.org/10.1038/s41586-023-06127-z.

17. Bérouti, M., Wagner, M., Greulich, W., Piseddu, I., Gärtig, J., Hansbauer, L., Müller-Hermes, C., Heiss, M., Pichler, A., Tölke, A.J., et al. (2025). Pseudouridine RNA avoids immune detection through impaired endolysosomal processing and TLR engagement. Cell *188*, 4880–4895.e15. https://doi.org/10.1016/j.cell.2025.05.032.

18. McLeod, C., Dymock, M., Flanagan, K.L., Plebanski, M., Marshall, H., Estcourt, M.J., Tjiam, M.C., Blyth, C.C., Subbarao, K., Mordant, F.L., et al. (2024). The Platform Trial In COVID-19 Priming and BOOsting (PICOBOO): The immunogenicity, reactogenicity, and safety of different COVID-19 vaccinations administered as a second booster (fourth dose) in AZD1222 primed individuals aged 50-<70 years old. J. Infect. *89*, 106286. https://doi.org/10.1016/j.jinf.2024.106286.

19. Chan, Y.K. (2024). A new immune pathway mediating AAV immune responses. Mol. Ther. *32*, 269–270. https://doi.org/10.1016/j.ymthe.2024.01.013.

20. Guo, Y., Chen, J., Ji, W., Xu, L., Xie, Y., He, S., Lai, C., Hou, K., Li, Z., Chen, G., and Wu, Z. (2023). High-titer AAV disrupts cerebrovascular integrity and induces lymphocyte infiltration in adult mouse brain. Mol. Ther. Methods Clin. Dev. *31*, 101102. https://doi.org/10.1016/j.omtm.2023.08.021.

Please cite this article in press as: Lainšček et al., Decoupling reactogenicity from efficacy enables safer mRNA vaccines, AAV gene delivery, and *in vivo* base editing, Molecular Therapy (2026), https://doi.org/10.1016/j.ymthe.2026.09.033

21. World Health Organization (2025). The selection and use of essential medicines, 2025: WHO Model List of Essential Medicines, 24th list (World Health Organization). https://doi.org/10.2471/B09474.

22. Rother, N., Yanginlar, C., Lindeboom, R.G.H., Bekkering, S., van Leent, M.M.T., Buijsers, B., Jonkman, I., de Graaf, M., Baltissen, M., Lamers, L.A., et al. (2020). Hydroxychloroquine Inhibits the Trained Innate Immune Response to Interferons. Cell Rep. Med. *1*, 100146. https://doi.org/10.1016/j.xcrm.2020.100146.

23. Kužnik, A., Benčina, M., Švajger, U., Jeras, M., Rozman, B., and Jerala, R. (2011). Mechanism of Endosomal TLR Inhibition by Antimalarial Drugs and Imidazoquinolines. J. Immunol. *186*, 4794–4804. https://doi.org/10.4049/jimmunol.1000702.

24. Faraone, I., Labanca, F., Ponticelli, M., De Tommasi, N., and Milella, L. (2020). Recent Clinical and Preclinical Studies of Hydroxychloroquine on RNA Viruses and Chronic Diseases: A Systematic Review. Molecules *25*, 5318. https://doi.org/10.3390/MOLECULES25225318.

25. Gupta, A., Andresen, J.L., Manan, R.S., and Langer, R. (2021). Nucleic acid delivery for therapeutic applications. Adv. Drug Deliv. Rev. *178*, 113834. https://doi.org/10.1016/j.addr.2021.113834.

26. Xu, J., Feng, H.T., Wang, C., Yip, K.H.M., Pavlos, N., Papadimitriou, J.M., Wood, D., and Zheng, M.H. (2003). Effects of Bafilomycin A1: an inhibitor of vacuolar H (+)-ATPases on endocytosis and apoptosis in RAW cells and RAW cell-derived osteoclasts. J. Cell. Biochem. *88*, 1256–1264. https://doi.org/10.1002/jcb.10477.

27. Kim, S., Jeon, J.H., Kim, M., Lee, Y., Hwang, Y.-H., Park, M., Li, C.H., Lee, T., Lee, J.-A., Kim, Y.-M., et al. (2024). Innate immune responses against mRNA vaccine promote cellular immunity through IFN-β at the injection site. Nat. Commun. *15*, 7226. https://doi.org/10.1038/s41467-024-51411-9.

28. Schrezenmeier, E., and Dörner, T. (2020). Mechanisms of action of hydroxychloroquine and chloroquine: implications for rheumatology. Nat. Rev. Rheumatol. *16*, 155–166. https://doi.org/10.1038/S41584-020-0372-X.

29. Liu, X., and Jusko, W.J. (2021). Physiologically Based Pharmacokinetics of Lysosomotropic Chloroquine in Rat and Human. J. Pharmacol. Exp. Ther. *376*, 261–272. https://doi.org/10.1124/jpet.120.000385.

30. Goody, S.M.G., Rowbottom, C., Liu, Y., and Chen, N. (2026). Biodistribution of mRNA vaccines in rats: Enrichment in injection site and lymph tissues and rapid clearance without tissue persistence. Mol. Ther. Nucleic Acids *37*, 102948. https://doi.org/10.1016/j.omtn.2026.102948.

31. Takanashi, A., Pouton, C.W., and Al-Wassiti, H. (2023). Delivery and Expression of mRNA in the Secondary Lymphoid Organs Drive Immune Responses to Lipid Nanoparticle-mRNA Vaccines after Intramuscular Injection. Mol. Pharm. *20*, 3876–3885. https://doi.org/10.1021/acs.molpharmaceut.2c01024.

32. Yoshimura, T., and Takahashi, M. (2007). IFN-gamma-mediated survival enables human neutrophils to produce MCP-1/CCL2 in response to activation by TLR ligands. J. Immunol. *179*, 1942–1949. https://doi.org/10.4049/jimmunol.179.3.1942.

33. Dai, J.-M., Zhang, X.-Q., Zhang, J.-J., Yang, W.-J., Yang, X.-M., Bian, H., and Chen, Z.-N. (2022). Blockade of mIL-6R alleviated lipopolysaccharide-induced systemic inflammatory response syndrome by suppressing NF-κB-mediated Ccl2 expression and inflammasome activation. MedComm *3*, e132. https://doi.org/10.1002/mco2.132.

34. Richard, S.A., Kampo, S., Hechavarria, M.E., Sackey, M., Buunaaim, A.D.B., Kuugbee, E.D., and Anabah, T.W. (2020). Elucidating the Pivotal Immunomodulatory and Anti-Inflammatory Potentials of Chloroquine and Hydroxychloroquine. J. Immunol. Res. *2020*, 4582612. https://doi.org/10.1155/2020/4582612.

35. Madhi, S.A., Baillie, V., Cutland, C.L., Voysey, M., Koen, A.L., Fairlie, L., Padayachee, S.D., Dheda, K., Barnabas, S.L., Bhorat, Q.E., et al. (2021). Efficacy of the ChAdOx1 nCoV-19 Covid-19 Vaccine against the B.1.351 Variant. N. Engl. J. Med. *384*, 1885–1898. https://doi.org/10.1056/nejmoa2102214.

36. Stone, D., Aubert, M., and Jerome, K.R. (2025). Adeno-associated virus vectors and neurotoxicity—lessons from preclinical and human studies. Gene Ther. *32*, 60–73. https://doi.org/10.1038/s41434-023-00405-1.

37. Suriano, C.M., Kumar, N., Verpeut, J.L., Ma, J., Jung, C., Dunn, C.E., Carvajal, B.V., Nguyen, A.V., and Boulanger, L.M. (2024). An innate immune response to adeno-associated virus genomes decreases cortical dendritic complexity and disrupts synaptic transmission. Mol. Ther. *32*, 1721–1738. https://doi.org/10.1016/j.ymthe.2024.03.036.

38. Foley, C.P., Rubin, D.G., Santillan, A., Sondhi, D., Dyke, J.P., Crystal, R.G., Gobin, Y.P., and Ballon, D.J. (2014). Intra-arterial delivery of AAV vectors to the mouse brain after mannitol mediated blood brain barrier disruption. J. Control Release *196*, 71–78. https://doi.org/10.1016/j.jconrel.2014.09.018.

39. Stone, D., Aubert, M., and Jerome, K.R. (2023). Breaching the blood-brain barrier: AAV triggers dose-dependent toxicity in the brain. Mol. Ther. Methods Clin. Dev. *31*, 101105. https://doi.org/10.1016/j.omtm.2023.09.001.

40. Rothgangl, T., Tálas, A., Ioannidi, E.I., Weber, Y., Böck, D., Matsushita, M., Villiger, E.A., Schmidheini, L., Moon, W.J., Lin, P.J.C., et al. (2025). Treatment of a metabolic liver disease in mice with a transient prime editing approach. Nat. Biomed. Eng. *9*, 1705–1718. https://doi.org/10.1038/s41551-025-01399-4.

41. Rothgangl, T., Dennis, M.K., Lin, P.J.C., Oka, R., Witzigmann, D., Villiger, L., Qi, W., Hruzova, M., Kissling, L., Lenggenhager, D., et al. (2021). In vivo adenine base editing of PCSK9 in macaques reduces LDL cholesterol levels. Nat. Biotechnol. *39*, 949–957. https://doi.org/10.1038/s41587-021-00933-4.

42. Hosseini-Kharat, M., Bremmell, K.E., and Prestidge, C.A. (2025). Why do lipid nanoparticles target the liver? Understanding of biodistribution and liver-specific tropism. Mol. Ther. Methods Clin. Dev. *33*, 101436. https://doi.org/10.1016/j.omtm.2025.101436.

43. Hooper, A.J., Tang, X.L., and Burnett, J.R. (2024). VERVE-101, a CRISPR base-editing therapy designed to permanently inactivate hepatic PCSK9 and reduce LDL-cholesterol. Expert Opin. Investig. Drugs *33*, 753–756. https://doi.org/10.1080/13543784.2024.2369747.

44. Musunuru, K., Grandinette, S.A., Wang, X., Hudson, T.R., Briseno, K., Berry, A.M., Hacker, J.L., Hsu, A., Silverstein, R.A., Hille, L.T., et al. (2025). Patient-Specific In Vivo Gene Editing to Treat a Rare Genetic Disease. N. Engl. J. Med. *392*, 2235–2243. https://doi.org/10.1056/NEJMoa2504747.

45. Brooks, D.L., Whittaker, M.N., Said, H., Dwivedi, G., Qu, P., Musunuru, K., Ahrens-Nicklas, R.C., Alameh, M.-G., and Wang, X. (2024). A base editing strategy using mRNA-LNPs for in vivo correction of the most frequent phenylketonuria variant. HGG Adv. *5*, 100253. https://doi.org/10.1016/j.xhgg.2023.100253.

46. Karikó, K., Buckstein, M., Ni, H., and Weissman, D. (2005). Suppression of RNA recognition by Toll-like receptors: the impact of nucleoside modification and the evolutionary origin of RNA. Immunity *23*, 165–175. https://doi.org/10.1016/J.IMMUNI.2005.06.008.

47. Chandler, L.C., Yusuf, I.H., McClements, M.E., Barnard, A.R., MacLaren, R.E., and Xue, K. (2020). Immunomodulatory Effects of Hydroxychloroquine and Chloroquine in Viral Infections and Their Potential Application in Retinal Gene Therapy. Int. J. Mol. Sci. *21*, 4972. https://doi.org/10.3390/ijms21144972.

48. Cenac, C., Ducatez, M.F., and Guéry, J.-C. (2022). Hydroxychloroquine inhibits proteolytic processing of endogenous TLR7 protein in human primary plasmacytoid dendritic cells. Eur. J. Immunol. *52*, 54–61. https://doi.org/10.1002/eji.202149361.

49. Rennen, S., Bosteels, V., De Nolf, C., Maréchal, S., Vetters, J., Van Lil, K., Webb, G., Swinnen, J., Van De Velde, E., Fayazpour, F., et al. (2025). Lipid nanoparticles as a tool to dissect dendritic cell maturation pathways. Cell Rep. *44*, 116150. https://doi.org/10.1016/j.celrep.2025.116150.

50. Hitti, E.G., Muazzen, Z., Moghrabi, W., Al-Yahya, S., and Khabar, K.S.A. (2024). Hydroxychloroquine attenuates double-stranded RNA-stimulated hyper-phosphorylation of tristetraprolin/ZFP36 and AU-rich mRNA stabilization. Immunology *173*, 511–519. https://doi.org/10.1111/imm.13835.

51. Gardet, A., Pellerin, A., McCarl, C.-A., Diwanji, R., Wang, W., Donaldson, D., Franchimont, N., Werth, V.P., and Rabah, D. (2019). Effect of in vivo Hydroxychloroquine and ex vivo Anti-BDCA2 mAb Treatment on pDC IFNα Production From Patients Affected With Cutaneous Lupus Erythematosus. Front. Immunol. *10*, 275. https://doi.org/10.3389/fimmu.2019.00275.

52. Loughrey, D., Paunovska, K., Echeverri, E.S., Tiegreen, K.E., and Dahlman, J.E. (2025). The time course of in vivo cellular responses to LNPs. Chem. Commun. *61*, 4535–4538. https://doi.org/10.1039/D4CC06659F.

Please cite this article in press as: Lainšček et al., Decoupling reactogenicity from efficacy enables safer mRNA vaccines, AAV gene delivery, and *in vivo* base editing, Molecular Therapy (2026), https://doi.org/10.1016/j.ymthe.2026.09.033

53. Belliveau, N.M., Huft, J., Lin, P.J., Chen, S., Leung, A.K., Leaver, T.J., Wild, A.W., Lee, J.B., Taylor, R.J., Tam, Y.K., et al. (2012). Microfluidic synthesis of highly potent limit-size lipid nanoparticles for in vivo delivery of siRNA. Mol. Ther. Nucleic Acids *1*, e37. https://doi.org/10.1038/mtna.2012.28.

54. Martin, M. (2011). Cutadapt removes adapter sequences from high-throughput sequencing reads. Embnet. J. *17*, 10–12. https://doi.org/10.14806/ej.17.1.200.

55. Bray, N.L., Pimentel, H., Melsted, P., and Pachter, L. (2016). Near-optimal probabilistic RNA-seq quantification. Nat. Biotechnol. *34*, 525–527. https://doi.org/10.1038/nbt.3519.

56. Love, M.I., Huber, W., and Anders, S. (2014). Moderated estimation of fold change and dispersion for RNA-seq data with DESeq2. Genome Biol. *15*, 550. https://doi.org/10.1186/s13059-014-0550-8.

57. Blighe, K., Rana, S., and Lewis, M. (2018). EnhancedVolcano: Publication-ready volcano plots with enhanced colouring and labeling. https://bioconductor.org/packages/release/bioc/vignettes/EnhancedVolcano/inst/doc/EnhancedVolcano.html.

58. Liao, Y., Wang, J., Jaehnig, E.J., Shi, Z., and Zhang, B. (2019). WebGestalt 2019: gene set analysis toolkit with revamped UIs and APIs. Nucleic Acids Res. *47*, W199–W205. https://doi.org/10.1093/nar/gkz401.

59. Monaco, G., Chen, H., Poidinger, M., Chen, J., de Magalhães, J.P., and Larbi, A. (2016). flowAI: automatic and interactive anomaly discerning tools for flow cytometry data. Bioinformatics *32*, 2473–2480. https://doi.org/10.1093/bioinformatics/btw191.

60. Lainšček, D., Fink, T., Forstnerič, V., Hafner-Bratkovič, I., Orehek, S., Strmšek, Ž., Manček-Keber, M., Pečan, P., Esih, H., Malenšek, Š., et al. (2021). A nanoscaffolded spike-rbd vaccine provides protection against sars-cov-2 with minimal anti-scaffold response. Vaccines *9*, 431. https://doi.org/10.3390/vaccines9050431.

61. Frey, A., Di Canzio, J., and Zurakowski, D. (1998). A statistically defined endpoint titer determination method for immunoassays. J. Immunol. Methods *221*, 35–41. https://doi.org/10.1016/S0022-1759(98)00170-7.